

Observational Strategies of CMB Temperature and Polarization Interferometry Experiments

Chan-Gyung Park¹, Kin-Wang Ng^{2,3}, Changbom Park¹, Guo-Chin Liu³, and Keiichi Umetsu³

ABSTRACT

We have simulated the interferometric observation of the Cosmic Microwave Background (CMB) temperature and polarization fluctuations. We have constructed data pipelines from the time-ordered raw visibility samples to the CMB power spectra which utilize the methods of data compression, maximum likelihood analysis, and optimal subspace filtering. They are customized for three observational strategies, such as the single pointing, the mosaicking, and the drift-scanning. For each strategy, derived are the optimal strategy parameters that yield band power estimates with minimum uncertainty. The results are general and can be applied to any close-packed array on a single platform such as the CBI and the forthcoming AMiBA experiments.

We have also studied the effect of rotation of the array platform on the band power correlation by simulating the CBI single pointing observation. It is found that the band power anti-correlations can be reduced by rotating the platform and thus densely sampling the visibility plane. This enables us to increase the resolution of the power spectrum in the ℓ -space down to the limit of the sampling theorem ($\Delta\ell = 226 \approx \pi/\theta$), which is narrower by a factor of about $\sqrt{2}$ than the resolution limit ($\Delta\ell \approx 300$) used in the recent CBI single pointing observation. The validity of this idea is demonstrated for a two-element interferometer that samples visibilities uniformly in the uv -annulus.

From the fact that the visibilities are the Fourier modes of the CMB field convolved with the beam, a fast unbiased estimator (FUE) of the CMB power spectra is developed and tested. It is shown that the FUE gives results very close to those from the quadratic estimator method without requiring large computer resources even though uncertainties in the results increase.

Subject headings: cosmic microwave background — cosmology: theory — techniques: interferometric

¹Astronomy Program, School of Earth and Environmental Sciences, Seoul National University, 151-742 Korea; parkc@astro.snu.ac.kr, cbp@astro.snu.ac.kr.

²Institute of Physics, Academia Sinica, Taipei, Taiwan 11529, R.O.C.; nkw@phys.sinica.edu.tw.

³Institute of Astronomy and Astrophysics, Academia Sinica, Taipei, Taiwan 11529, R.O.C.; gcliu@asiaa.sinica.edu.tw, keiichi@asiaa.sinica.edu.tw.

1. Introduction

It is theoretically expected that the CMB is polarized. The CMB quadrupole anisotropy causes CMB photons polarized by Thomson scattering with electrons at the last scattering surface ($z \simeq 1,100$) and during the reionization epoch ($z \lesssim 7$) (Hu & White 1997). The amplitude of polarization is predicted to be 1 – 10% of that of the temperature anisotropies, depending on angular scales. The CMB polarization can provide useful information that is not much contained in the temperature anisotropy, such as the epoch of reionization or the tensor perturbations. Recently Keating et al. (2001) have reported the result of the POLAR experiment, giving upper limit of order 10 μ K on the large-scale CMB polarization. The PIQUE experiment (Hedman et al. 2001, 2002) have also obtained a similar upper limit at subdegree scales. De Oliveira-Costa et al. (2002) have tried to measure the cross-correlation C_ℓ^{TE} between temperature and E -mode polarization power spectra by cross-correlating the PIQUE and Saskatoon data (Netterfield et al. 1997). Many single dish and interferometry experiments such as MAXIPOL, POLAR, Polatron, COMPOSAR, CMB RoPE, DASI, and CBI are on-going to detect these faint polarized signals of CMB origin. Very recently, the DASI has reported a detection of the CMB E -mode polarization and the TE cross-correlation by differencing the CMB fluctuations in two fields in 271 days of observation (Leitch et al. 2002b; Kovac et al. 2002).

Since the Cambridge Anisotropy Telescope has detected the anisotropy on subdegree scales (CAT; O’Sullivan et al. 1995; Scott et al. 1996), the Degree Angular Scale Interferometer (DASI; Leitch et al. 2002a; Halverson et al. 2002), the Cosmic Background Imager (CBI⁴; Padin et al. 2001; Mason et al. 2002; Pearson et al. 2002), and the Very Small Array (VSA; Taylor et al. 2002; Scott et al. 2002) have also measured the CMB angular power spectrum down to subdegree scales. A desirable feature of the interferometer for CMB observation is that it directly measures the power spectrum, and that the polarimetry is a routine. In addition, many systematic problems that are inherent in single-dish experiments, such as the ground and near field atmospheric pickup and spurious polarization signals, can be significantly reduced.

The observation of CMB polarization using close-packed interferometers are also on-going or planned by the experiments like the DASI, CBI, and the forthcoming interim Array for Microwave Background Anisotropy (AMiBA⁵; Lo et al. 2001). They have full capabilities to probe the CMB temperature and polarization simultaneously. The feed horns are able to detect T , Q , U , and V Stokes parameters using complex linear or circular polarizers, aiming to detect CMB linear (Q and U) polarization at wave numbers $100 \lesssim \ell \lesssim 4,000$.

This paper proposes the data analysis techniques for various strategies of the interferometric observation, especially when the uv -space beam size is larger than the structures of the CMB power spectrum in the ℓ -space. An attempt is made to increase the resolution of the estimated power

⁴<http://www.astro.caltech.edu/~tjp/CBI>

⁵<http://www.asiaa.sinica.edu.tw/amiba>

spectrum in the ℓ -space. We have adopted three observational strategies, namely single pointing, mosaicking, and drift-scanning methods, and tested a few analysis methods extracting the angular power spectra from mock data for efficiency.

The outline of this paper is as follows. In §2 and §3, beginning with a summary of CMB interferometric observation, we describe a theoretical formalism for analyzing CMB interferometric data. A prescription for making mock CMB observations with interferometric array is given. Application of each observational strategy is made in §4. A fast unbiased power spectrum estimator is introduced in §5. Finally, the summary and discussion are given in §6.

2. CMB Interferometry Experiment

2.1. Visibility

Here we briefly summarize the CMB interferometry experiments (Hobson, Lasenby, & Jones 1995; Hobson & Masinger 2002, hereafter HM02; White et al. 1999a, hereafter W99). Only the observed CMB signal and instrument noise are considered, and other contaminations like the ground pickup or Galactic foregrounds are not taken into account. The sky is assumed to be flat since the field size surveyed by the interferometric array is usually smaller than 10° .

The visibility function of CMB temperature fluctuations sampled at a pointing position \mathbf{y}_m on the sky is the Fourier transform of the temperature anisotropy $\Delta T(\mathbf{x})$ on the sky weighted by the primary beam $A(\mathbf{x} - \mathbf{y}_m, \nu)$, i.e.,

$$V_{\mathbf{y}_m}^T(\mathbf{u}, \nu) = \frac{\partial B_\nu}{\partial T} \int d^2x A(\mathbf{x} - \mathbf{y}_m, \nu) \Delta T(\mathbf{x}) e^{i2\pi \mathbf{u} \cdot \mathbf{x}} \quad (1)$$

(Hobson et al. 1995; W99). The factor $\partial B_\nu / \partial T \equiv (2k_B^3 T^2 / c^2 h^2) x^4 e^x / (e^x - 1)^2$ is the conversion factor from temperature to intensity, where $B_\nu(T)$ is the Planck function, k_B is the Boltzmann's constant, h is the Planck constant, c is the speed of light, and $x \equiv h\nu / k_B T$. We assume $T \simeq T_{\text{CMB}} = 2.725 \pm 0.002$ K (Mather et al. 1999). The *baseline vector* \mathbf{u} is a variable conjugate to the coordinate \mathbf{x} , and has a dimension of the inverse angle. In practice a vector connecting two centers of a pair of dishes determines a baseline vector \mathbf{u} in unit of observing wavelength. For a small field, $u = \frac{1}{2} \cot(\pi/\ell) \approx \ell/2\pi$ (Hobson & Magueijo 1996). Each frequency channel gives an independent set of visibility samples with different baseline vectors.

The size of the primary beam $A(\mathbf{x})$ determines the area of the sky that is viewed and hence the size of the map while the maximum spacing of the array determines the resolution. $A(\mathbf{x})$ is normalized to unity at the pointing center, $A(0) = 1$. The visibility in equation (1) can be also defined in the uv -domain,

$$V_{\mathbf{y}_m}^T(\mathbf{u}, \nu) = \frac{\partial B_\nu}{\partial T} \int d^2w \tilde{A}(\mathbf{w}, \nu) e^{i2\pi \mathbf{w} \cdot \mathbf{y}_m} \Delta \tilde{T}(\mathbf{u} - \mathbf{w}), \quad (2)$$

where $\tilde{A}(\mathbf{u}, \nu)$ and $\Delta\tilde{T}(\mathbf{u})$ are Fourier transform pairs of $A(\mathbf{x}, \nu)$ and $\Delta T(\mathbf{x})$, respectively. Let us define the generalized uv -space beam pattern $\tilde{A}_{\mathbf{y}_m}(\mathbf{u}, \nu)$ at a pointing position \mathbf{y}_m from the phase reference point,

$$\tilde{A}_{\mathbf{y}_m}(\mathbf{u}, \nu) \equiv \tilde{A}(\mathbf{u}, \nu) e^{i2\pi\mathbf{u}\cdot\mathbf{y}_m}. \quad (3)$$

We adopt a beam pattern $\tilde{A}(\mathbf{u}, \nu)$ given by W99,

$$\tilde{A}(\mathbf{u}, \nu) = \frac{8}{\pi^2 D_\lambda^2} \left(\arccos \left(\frac{u}{D_\lambda} \right) - \frac{u}{D_\lambda} \sqrt{1 - \left(\frac{u}{D_\lambda} \right)^2} \right), \quad (4)$$

where D_λ is the diameter of a dish (D) in unit of wavelength. It is defined by the autocorrelation of the electric field pattern of the flat-illuminated feed horn. This is equal to the autocorrelation of a pillbox of radius $D_\lambda/2$ (van Waerbeke 2000). The primary beam pattern $A(\mathbf{x})$ obtained by the inverse Fourier transform of equation (4) is well approximated by a Gaussian function (for instance, FWHM $\simeq 20'$ for a dish with $D = 60$ cm and the center frequency $\nu_0 = 95$ GHz).

Visibilities of CMB Q and U Stokes parameters, $V_{\mathbf{y}_m}^Q$ and $V_{\mathbf{y}_m}^U$, can be similarly defined by replacing $\Delta T(\mathbf{x})$ with $Q(\mathbf{x})$ and $U(\mathbf{x})$, respectively. The Q and U Stokes parameters depend on the observer's coordinate system. Under a rotation of coordinate system by ψ on the sky, $Q \pm iU$ transforms as a spin-2 tensor, $(Q \pm iU) \rightarrow e^{\mp 2i\psi} (Q \pm iU)$ (Zaldarriaga & Seljak 1997). It is useful to deal with rotationally invariant polarization quantities, known as E - and B -mode polarizations. We follow the small-scale approximation of Seljak (1997) and Zaldarriaga & Seljak (1997) to describe CMB temperature and polarization fields,

$$\begin{aligned} \Delta T(\mathbf{x}) &= \int d^2u \, \Delta\tilde{T}(\mathbf{u}) e^{-i2\pi\mathbf{u}\cdot\mathbf{x}}, \\ Q(\mathbf{x}) &= \int d^2u \, [\tilde{E}(\mathbf{u}) \cos 2\phi_{\mathbf{u}} - \tilde{B}(\mathbf{u}) \sin 2\phi_{\mathbf{u}}] e^{-i2\pi\mathbf{u}\cdot\mathbf{x}}, \\ U(\mathbf{x}) &= \int d^2u \, [\tilde{E}(\mathbf{u}) \sin 2\phi_{\mathbf{u}} + \tilde{B}(\mathbf{u}) \cos 2\phi_{\mathbf{u}}] e^{-i2\pi\mathbf{u}\cdot\mathbf{x}}, \end{aligned} \quad (5)$$

where $\tilde{E}(\mathbf{u})$ and $\tilde{B}(\mathbf{u})$ are the Fourier transforms of the E - and B -mode polarization fields, and $\phi_{\mathbf{u}}$ is the direction angle of \mathbf{u} .

2.2. Visibility Covariance Matrix

We are interested in measuring the angular power spectra of the CMB temperature fluctuations ($\mathcal{C}_\ell^{TT} \equiv \ell(\ell+1)C_\ell^{TT}/2\pi$), polarizations (\mathcal{C}_ℓ^{EE} and \mathcal{C}_ℓ^{BB}), and their cross-correlation (\mathcal{C}_ℓ^{TE}). We can relate them with the power spectrum $S(u)$ defined in the uv -plane under the flat-sky approximation by, for example, $\ell(\ell+1)C_\ell^{TE}/2\pi \approx 2\pi u^2 S_{TE}(u)$ where $S_{TE}(u)$ is defined by $\langle \Delta\tilde{T}(\mathbf{u}) \tilde{E}^*(\mathbf{v}) \rangle = S_{TE}(u) \delta(\mathbf{u} - \mathbf{v})$, and likewise for other components.

To estimate CMB temperature and polarization power spectra from the visibility data using the maximum likelihood analysis, it is essential to construct visibility covariance matrices. Combining equations (2) and (5) gives the visibility covariance matrix,

$$\begin{aligned} M_{mn}^{ij} &\equiv \langle V_{\mathbf{y}_m}^X(\mathbf{u}_i, \nu_i) V_{\mathbf{y}_n}^{Y*}(\mathbf{u}_j, \nu_j) \rangle \\ &= \frac{\partial B_{\nu_i}}{\partial T} \frac{\partial B_{\nu_j}}{\partial T} \int d^2w \tilde{A}_{\mathbf{y}_m}(\mathbf{u}_i - \mathbf{w}, \nu_i) \tilde{A}_{\mathbf{y}_n}^*(\mathbf{u}_j - \mathbf{w}, \nu_j) \mathcal{S}_{XY}(\mathbf{w}), \end{aligned} \quad (6)$$

where X and Y correspond to T , Q , or U , and i (j) is a visibility data index at a pointing position \mathbf{y}_m (\mathbf{y}_n). All possible combinations of $\mathcal{S}_{XY}(\mathbf{w})$, defined by $\langle \tilde{X}(\mathbf{v}) \tilde{Y}^*(\mathbf{w}) \rangle = \mathcal{S}_{XY}(\mathbf{w}) \delta(\mathbf{v} - \mathbf{w})$, are listed in Table 1. We assume no correlation of temperature and E -mode polarization with B -mode, which is expected in common inflationary scenarios (Hu & White 1997). Changing the sign of \mathbf{u}_j in equation (6) gives another complex covariance matrix,

$$\begin{aligned} N_{mn}^{ij} &\equiv \langle V_{\mathbf{y}_m}^X(\mathbf{u}_i, \nu_i) V_{\mathbf{y}_n}^Y(\mathbf{u}_j, \nu_j) \rangle \\ &= \frac{\partial B_{\nu_i}}{\partial T} \frac{\partial B_{\nu_j}}{\partial T} \int d^2w \tilde{A}_{\mathbf{y}_m}(\mathbf{u}_i - \mathbf{w}, \nu_i) \tilde{A}_{\mathbf{y}_n}(\mathbf{u}_j + \mathbf{w}, \nu_j) \mathcal{S}_{XY}(\mathbf{w}). \end{aligned} \quad (7)$$

In practice, it is more convenient to use real quantities rather than complex ones. Separating the complex visibilities into real (V^R) and imaginary (V^I) parts and combining M_{mn}^{ij} and N_{mn}^{ij} appropriately, we obtain the followings (HM02, Appendix A),

$$\begin{aligned} \langle V_{\mathbf{y}_m}^R(\mathbf{u}_i, \nu_i) V_{\mathbf{y}_n}^R(\mathbf{u}_j, \nu_j) \rangle &= (\text{Re}[M_{mn}^{ij}] + \text{Re}[N_{mn}^{ij}])/2, \\ \langle V_{\mathbf{y}_m}^I(\mathbf{u}_i, \nu_i) V_{\mathbf{y}_n}^I(\mathbf{u}_j, \nu_j) \rangle &= (\text{Re}[M_{mn}^{ij}] - \text{Re}[N_{mn}^{ij}])/2, \\ \langle V_{\mathbf{y}_m}^R(\mathbf{u}_i, \nu_i) V_{\mathbf{y}_n}^I(\mathbf{u}_j, \nu_j) \rangle &= (-\text{Im}[M_{mn}^{ij}] + \text{Im}[N_{mn}^{ij}])/2, \\ \langle V_{\mathbf{y}_m}^I(\mathbf{u}_i, \nu_i) V_{\mathbf{y}_n}^R(\mathbf{u}_j, \nu_j) \rangle &= (\text{Im}[M_{mn}^{ij}] + \text{Im}[N_{mn}^{ij}])/2. \end{aligned} \quad (8)$$

2.3. Simulated Observations

We use the CMBFAST power spectra C_ℓ^{TT} , C_ℓ^{EE} , and the cross-correlation C_ℓ^{TE} (Seljak & Zaldarriaga 1996; Zaldarriaga, Seljak, & Bertschinger 1998) of a flat Λ CDM cosmological model. The model parameters are $\Omega = 1$, $\Omega_\Lambda = 0.7$, $h = 0.82$, $\Omega_b h^2 = 0.03$, and $n_s = 0.975$, which was given by the joint MAXIMA-BOOMERANG data analysis (Jaffe et al. 2001). We assume that the B -mode vanishes ($\tilde{B}(\mathbf{u}) = 0$). To generate ΔT , Q and U fields on a patch of the sky we use the Fourier transform relations in equation (5). For a given ℓ we construct a 2×2 matrix \mathbf{M} that has C_ℓ^{TT} and C_ℓ^{EE} as the diagonal and C_ℓ^{TE} as the off-diagonal elements. We then Cholesky-decompose this matrix, $\mathbf{M} = \mathbf{L}\mathbf{L}^T$, where \mathbf{L} is a lower triangular matrix, and assign random fluctuations $\Delta\tilde{T}(\mathbf{u})$ and $\tilde{E}(\mathbf{u})$ in each uv -cell using the following relation,

$$\begin{pmatrix} \Delta\tilde{T}(\mathbf{u}) \\ \tilde{E}(\mathbf{u}) \end{pmatrix} = \mathbf{L} \begin{pmatrix} r_1 \\ r_2 \end{pmatrix}. \quad (9)$$

Here r_1 and r_2 are random complex numbers drawn from the Gaussian distribution with zero mean and unit variance (for definite normalization of Eq. 9 in a finite field, see Wu 1999). The results are inverse Fourier transformed (Eq. 5) to yield $\Delta T(\mathbf{x})$, $Q(\mathbf{x})$, and $U(\mathbf{x})$. These fields are then multiplied by the primary beam and Fourier transformed to give a regular array of visibilities (Eq. 1). An observation is simulated by sampling the regular array at the \mathbf{u} points specified by the dish configuration and observation strategy. The bilinear interpolation is used in the sampling.

The instrument noise is simulated by adding a random complex number to each visibility whose real and imaginary parts are drawn from a Gaussian distribution with the variance of the noise predicted in a real observation. We use the sensitivity per baseline per polarization defined as (Wrobel & Walker 1999; Ng 2001)

$$s_b = \frac{1}{\eta_s \eta_a} \frac{2k_B T_{sys}}{A_{phys}} \frac{1}{\sqrt{2\Delta\nu}}, \quad (10)$$

where $\Delta\nu$ is the bandwidth, A_{phys} is the physical area of an elemental aperture, T_{sys} is the system noise temperature, and η_s (η_a) is the system (aperture) efficiency. We assume $\eta_s = \eta_a = 0.8$. Equation (10) is the sensitivity of a simple interferometer with a single real output consisting of the product of the voltages from two antennae. For a complex correlator, the noise is statistically the same in each of the two channels and thus the real and imaginary correlator outputs, σ_r and σ_i respectively, are equal with $\sigma_r = \sigma_i = \sigma_b$, where $\sigma_b = s_b/\sqrt{\tau_{acc}}$ and τ_{acc} is the correlator accumulation time. If we use the simultaneous dual polarizer with noise level σ_b per polarization, the T , Q , and U visibilities will obey Gaussian statistics characterized by zero means and standard deviations, $\sigma_T = \sigma_Q = \sigma_U = \sigma_b/\sqrt{2}$.

The instrumental noise of a single dish experiment has a strong correlation with itself, for instance due to the $1/f$ noise statistics. But the noise of an interferometric array is randomly distributed over the baselines and observations. This is because the noise in each correlator output of a pair of dishes has independent random noise statistics. Therefore, the noise covariance matrix of the visibility data can be assumed to be diagonal, with the non-zero element simply given by the variance of the noise of each baseline component.

3. Data Analysis

3.1. Power Spectrum Estimation

We summarize the basic scheme for the quadratic estimator of the CMB power spectrum based on the maximum likelihood analysis (Bond, Jaffe, & Knox 1998; Tegmark 1997b; Tegmark & de Oliveira-Costa 2001).

We construct the data vector $\mathbf{V} = (\mathbf{V}^T, \mathbf{V}^Q, \mathbf{V}^U)$, with each visibility data point decomposed into real and imaginary parts. The observed visibility is the sum of contributions from the CMB signal and the instrument noise, $V_i = V_{Si} + n_i$ ($i = 1, 2, \dots, N_p$), where N_p is the number of data

points including all the real and imaginary components of T , Q , and U visibilities. The covariance matrix of the visibility data becomes

$$C_{ij} = \langle V_i V_j \rangle = \langle V_{Si} V_{Sj} \rangle + \langle n_i n_j \rangle = S_{ij} + N_{ij}. \quad (11)$$

The S_{ij} and N_{ij} are called signal and noise covariance matrices, respectively, and the CMB signal is assumed to be uncorrelated with the instrument noise. The matrix element S_{ij} is obtained from equation (8), where we perform numerical integrations in equations (6) and (7). Assuming that the CMB T , Q , and U fields are multivariate Gaussian random variables, we get a maximum likelihood function,

$$\mathcal{L}(\{\mathcal{C}_b\}) = \frac{1}{(2\pi)^{N_p/2} |\mathbf{C}|^{1/2}} \exp(-\mathbf{V}^T \mathbf{C}^{-1} \mathbf{V}/2) \quad (12)$$

for a given set of parameters $\{\mathcal{C}_b\} = \{\mathcal{C}_1^{TT}, \dots, \mathcal{C}_{N_b/3+1}^{EE}, \dots, \mathcal{C}_{2N_b/3+1}^{TE}, \dots, \mathcal{C}_{N_b}^{TE}\}$. Here the $\mathcal{C}_b \equiv 2\pi u_b^2 S(u_b)$ is an estimate of band power for a band centered on u_b ($b = 1, 2, \dots, N_b$), and N_b is the total number of measured band powers. The superscript T denotes transpose of a vector. By using the Newton-Raphson method, after several iterations we can find a set of band powers that most likely fit the simulated data of the assumed cosmological model and thus maximize the likelihood function. The full quadratic estimator is

$$\begin{aligned} \delta \mathcal{C}_b &= \sum_{b'} (\mathbf{F}^{-1})_{bb'} \frac{\partial \ln \mathcal{L}}{\partial \mathcal{C}_{b'}} \\ &= \frac{1}{2} \sum_{b'} (\mathbf{F}^{-1})_{bb'} \text{Tr} \left[(\mathbf{V} \mathbf{V}^T - \mathbf{C}) \mathbf{C}^{-1} \frac{\partial \mathbf{S}}{\partial \mathcal{C}_{b'}} \mathbf{C}^{-1} \right], \end{aligned} \quad (13)$$

where the $N_b \times N_b$ matrix \mathbf{F} is the Fisher information matrix defined as

$$F_{bb'} \equiv - \left\langle \frac{\partial^2 \ln \mathcal{L}}{\partial \mathcal{C}_b \partial \mathcal{C}_{b'}} \right\rangle = \frac{1}{2} \text{Tr} \left(\mathbf{C}^{-1} \frac{\partial \mathbf{S}}{\partial \mathcal{C}_b} \mathbf{C}^{-1} \frac{\partial \mathbf{S}}{\partial \mathcal{C}_{b'}} \right). \quad (14)$$

The square root of the diagonal component of the inverse Fisher matrix, $(\mathbf{F}^{-1})_{bb}^{1/2}$, is the minimum standard deviation of the measured band power \mathcal{C}_b . The derivative of the signal covariance matrix with respect to a band power estimate, $\partial \mathbf{S} / \partial \mathcal{C}_b$, is obtained by combining $\partial M_{mn}^{ij} / \partial \mathcal{C}_b$ and $\partial N_{mn}^{ij} / \partial \mathcal{C}_b$ as in equation (8). For a band power of temperature anisotropy (\mathcal{C}_b^{TT}) with a band width ranging from $|\mathbf{u}_{b1}|$ to $|\mathbf{u}_{b2}|$, for example,

$$\frac{\partial M_{mn}^{ij}}{\partial \mathcal{C}_b^{TT}} = \frac{\partial B_{\nu_i}}{\partial T} \frac{\partial B_{\nu_j}}{\partial T} \int_0^{2\pi} \frac{d\theta_w}{2\pi} \int_{|\mathbf{u}_{b1}|}^{|\mathbf{u}_{b2}|} \frac{dw}{w} \tilde{A}_{\mathbf{y}_m}(\mathbf{u}_i - \mathbf{w}, \nu_i) \tilde{A}_{\mathbf{y}_n}^*(\mathbf{u}_j - \mathbf{w}, \nu_j), \quad (15)$$

and likewise for $\partial N_{mn}^{ij} / \partial \mathcal{C}_b^{TT}$. Cosine or sine factors are included in the integrand for band powers of polarization and cross-correlation (\mathcal{C}_b^{EE} and \mathcal{C}_b^{TE}).

For comparing a set of measured band powers $\{\mathcal{C}_b\}$ with cosmological models, we require a route to get band power expectation values $\langle \mathcal{C}_b \rangle$ from the model power spectrum \mathcal{C}_ℓ . The expectation value for a band power spectrum estimate \mathcal{C}_b is given by

$$\langle \mathcal{C}_b \rangle = \sum_{b'} (\mathbf{F}^{-1})_{bb'} \sum_{\ell \in \text{all}, \ell' \in b'} \mathcal{C}_\ell F_{\ell\ell'}^s = \sum_{\ell} \left(W_\ell^b / \ell \right) \mathcal{C}_\ell, \quad (16)$$

where \mathbf{F} is the band-power Fisher matrix, and the $F_{\ell\ell'}^s$ is a Fisher matrix element with bands of the individual multipoles. W_ℓ^b/ℓ is called the band power window function (Knox 1999; Pryke et al. 2002), and defined as

$$W_\ell^b/\ell \equiv \sum_{b'} (\mathbf{F}^{-1})_{bb'} \sum_{\ell' \in b'} F_{\ell\ell'}^s, \text{ and } \sum_{\ell} W_\ell^b/\ell = 1. \quad (17)$$

This function can be considered as a filter that averages out the power spectrum with variance weighting scheme (see Tegmark 1997b; Tegmark & de Oliveira-Costa 2001 for a related discussion).

Although the quadratic estimator is much faster than the direct evaluation of the likelihood function in finding the maxima, it still demands intensive computing power. The most time consuming part is the calculation of \mathbf{F} , which is $\mathcal{O}(N_p^3)$ operation. The visibility data obtained from mosaicking or drift-scanning usually involves a large amount of visibilities, but many of them are strongly correlated. One way to increase the efficiency of the calculation is to work with a subset of the data that contains most of the signal. This transformation can be obtained using the *optimal subspace filtering*, also known as the signal-to-noise eigenmode transform (see Tegmark, Taylor, & Heavens 1997 for a review). In this paper we follow the transformation method given by Bond et al. (1998, Appendix A). We first perform a whitening transformation,

$$\begin{aligned} \mathbf{N} &\longrightarrow \mathbf{N}^{-1/2} \mathbf{N} \mathbf{N}^{-1/2} = \mathbf{I}, \\ \mathbf{S} &\longrightarrow \mathbf{N}^{-1/2} \mathbf{S} \mathbf{N}^{-1/2}, \\ \mathbf{V} &\longrightarrow \mathbf{N}^{-1/2} \mathbf{V}, \end{aligned} \quad (18)$$

where the whitening filter $\mathbf{N}^{-1/2}$ is the inverse of the Cholesky decomposition of \mathbf{N} . Since \mathbf{N} is diagonal, the above quantities reduce to simple forms, δ_{ij} , $S_{ij}/\sigma_i\sigma_j$, and V_i/σ_i , respectively. By diagonalizing the signal covariance matrix using the similarity transformation, we get

$$\begin{aligned} \mathbf{S} &\longrightarrow \mathbf{R}^T (\mathbf{N}^{-1/2} \mathbf{S} \mathbf{N}^{-1/2}) \mathbf{R} = \boldsymbol{\varepsilon} = \text{diag}(\varepsilon_k), \\ \mathbf{V} &\longrightarrow \mathbf{R}^T (\mathbf{N}^{-1/2} \mathbf{V}) = \mathbf{V}^\varepsilon, \end{aligned} \quad (19)$$

where diagonal components of $\boldsymbol{\varepsilon}$ are eigenvalues of the whitened signal covariance matrix, and \mathbf{R} is an unitary matrix of which the k th column vector is an eigenvector corresponding to the k th eigenvalue ε_k . Transformation of $\partial\mathbf{S}/\partial\mathcal{C}_b$ into the eigenbasis can be also performed in a similar way. In this new basis, the data V_k^ε 's are uncorrelated variables with variances $\langle V_k^{\varepsilon 2} \rangle = 1 + \varepsilon_k$. The ε_k 's are usually called the signal-to-noise eigenmodes. In our analysis, we can keep only the top 20 – 30% of the modes and treat them as a new data set. This is an excellent approximation to the original dataset because the contribution of eigenmodes with lower signal-to-noise ratios to the CMB signal is relatively negligible. By replacing the covariance matrix and the data vector in equations (13) and (14) with the transformed ones in equation (19), we get a new version of quadratic estimator in this eigenmode basis (see Eqs. A10 and A11 of Bond et al. 1998). Although in this formalism the transformation into the signal-to-noise basis, which is $\mathcal{O}(N_p^3)$ operation, is the most expensive part, the remaining procedures do not require large computation.

3.2. Data Compression: Pixelization in real- and uv -spaces

It is essential to compress the visibility data, since the quadratic estimator for power spectrum requires very large operation proportional to $\mathcal{O}(N_p^3)$. The optimal subspace filtering described in §3.1 is one method for data compression. For a completely close-packed array, we can reduce the length of the data set by averaging all the visibilities with the same baseline vector for each component (T , Q , U) and observing frequency. For example, the 7-element AMiBA in hexagonal configuration gives 21 baselines for each frequency channel, and they can be reduced to 9 independent baselines (Fig. 1a).

In many CMB experiments, a telescope scans the sky continuously many times over a specified survey area, and generates the time-ordered data stream. Analyzing this raw data directly to estimate cosmological parameters is intractable. The same problem arises in the drift-scanning mode of the CMB interferometric observation (see §4.3). Furthermore, if the platform of the interferometer rotates with respect to the survey field during the observation we will get a even larger visibility data set from a denser coverage of the uv -plane with the moving baseline vectors. In this case pixelization in the real- and/or uv -spaces can serve as a data compression method (Wu 2002). HM02 have developed a pixelization scheme in the uv -plane (see also Myers et al. 2002). This can be understood as a commonly-used map-making process (Tegmark 1997a; Stompor et al. 2002). Here we generalize the uv -space pixelization method of HM02 to include the real-space pixelization as well.

The time-ordered visibility data obtained by an interferometric array can be modeled by the pixelized visibility data vector \mathbf{V}^{pix} multiplied by a pointing matrix \mathbf{A} plus a time-ordered instrumental noise vector \mathbf{n} ,

$$\mathbf{V}^{\text{tod}} = \mathbf{A}\mathbf{V}^{\text{pix}} + \mathbf{n}. \quad (20)$$

In component notation it is

$$V_{\mathbf{y}(t_i)}^{\text{tod}}(\mathbf{u}_k) = \sum_{p,l} A_{(ik)(pl)} V_{\mathbf{y}_p}^{\text{pix}}(\mathbf{u}_l) + n_{\mathbf{y}(t_i)}(\mathbf{u}_k), \quad (21)$$

where $\mathbf{y}(t_i)$ and \mathbf{u}_k are the observing position and the baseline vector at time t_i , and \mathbf{y}_p and \mathbf{u}_l are the pixelized real- and uv -space positions, respectively. The pointing matrix \mathbf{A} is determined entirely by the observational or scanning scheme. Suppose that the total number of time-ordered visibility data at a frequency ν is N_{tod} , and the length of the pixelized visibility is N_{pix} . Then the $N_{\text{tod}} \times N_{\text{pix}}$ pointing matrix \mathbf{A} is defined with matrix elements $A_{(ik)(pl)} = 1$ if $(\mathbf{y}(t_i), \mathbf{u}_k)$ lies in the cell specified by $(\mathbf{y}_p, \mathbf{u}_l)$, otherwise $A_{(ik)(pl)} = 0$.

The noise covariance matrix of the time-ordered visibility data can be taken to be diagonal (see §2.3),

$$(\mathbf{N}_t)_{(ik)(i'k')} = \langle n_{\mathbf{y}(t_i)}(\mathbf{u}_k) n_{\mathbf{y}(t_{i'})}(\mathbf{u}_{k'}) \rangle = \sigma_{ik}^2 \delta_{ii'} \delta_{kk'}. \quad (22)$$

A solution $\tilde{\mathbf{V}}^{\text{pix}}$ of equation (20) can be obtained by applying appropriate filtering matrix \mathbf{W} , i.e.,

$$\tilde{\mathbf{V}}^{\text{pix}} = \mathbf{W}\mathbf{V}^{\text{tod}}. \quad (23)$$

We adopt the well-known minimum-variance filter (Janssen & Gulkis 1992; Tegmark 1997a),

$$\mathbf{W} = (\mathbf{A}^T \mathbf{N}_t^{-1} \mathbf{A})^{-1} \mathbf{A}^T \mathbf{N}_t^{-1}. \quad (24)$$

This filter has an attractive property that the reconstruction error, $\delta \mathbf{V}_e \equiv \tilde{\mathbf{V}}^{\text{pix}} - \mathbf{V}^{\text{pix}} = (\mathbf{A}^T \mathbf{N}_t^{-1} \mathbf{A})^{-1} \mathbf{A}^T \mathbf{N}_t^{-1} \mathbf{n}$, becomes independent of \mathbf{V}^{pix} . The noise covariance matrix in the pixelized visibility data becomes

$$\mathbf{N}_p \equiv \langle \delta \mathbf{V}_e \delta \mathbf{V}_e^T \rangle = (\mathbf{A}^T \mathbf{N}_t^{-1} \mathbf{A})^{-1}. \quad (25)$$

Generally, the reconstructed visibility $\tilde{\mathbf{V}}^{\text{pix}}$ is the minimum-variance estimate of \mathbf{V}^{pix} , and becomes maximum-likelihood estimate provided that the probability distribution of \mathbf{n} is Gaussian. Since the time-ordered noise covariance matrix \mathbf{N}_t is diagonal, the matrix equations for the pixelized visibility and its noise covariance (Eqs. 23 and 25) are simple bin-averaging processes, i.e.,

$$\tilde{V}_{\mathbf{y}_p}^{\text{pix}}(\mathbf{u}_l) = \frac{\sum_{i \in p, k \in l} V_{\mathbf{y}(t_i)}^{\text{tod}}(\mathbf{u}_k) / \sigma_{ik}^2}{\sum_{i \in p, k \in l} 1 / \sigma_{ik}^2}, \quad (26)$$

and

$$(\mathbf{N}_p)_{(pl)(p'l')} = \left\{ 1 / \sum_{i \in p, k \in l} 1 / \sigma_{ik}^2 \right\} \delta_{pp'} \delta_{ll'}. \quad (27)$$

From equations (23) and (24) it can be understood that when \mathbf{W} acts on \mathbf{V}^{tod} , the first operation $\mathbf{A}^T \mathbf{N}_t^{-1} \mathbf{V}^{\text{tod}}$ maps the raw data into the pixelized visibility space; this step averages all data with coordinates $(\mathbf{y}(t_i), \mathbf{u}_k)$ that belong to the cell $(\mathbf{y}_p, \mathbf{u}_l)$, weighed with noise variance σ_{ik}^2 . The second one, $(\mathbf{A}^T \mathbf{N}_t^{-1} \mathbf{A})^{-1}$, is simply the normalization factor.

The remaining issue is to determine the size of the pixel (both in real- and uv -spaces) before processing equations (26) and (27). In virtue of the sampling theorem the size of the uv -pixel, Δu_{pix} , must not be bigger than a half of the FWHM of the beam, i.e., $\Delta u_{\text{pix}} \lesssim \Delta u_{\text{fwhm}}/2$ (Hobson et al. 1995; HM02). For single pointing observation, the half-width of the beam defined in equation (4) is given by

$$\Delta u_{\text{fwhm}}/2 \simeq 12 \left(\frac{D}{30 \text{ cm}} \right) \left(\frac{\nu}{30 \text{ GHz}} \right). \quad (28)$$

For example, $\Delta u_{\text{fwhm}}/2 \simeq 36$ for the CBI ($D = 90 \text{ cm}$, $\nu_0 \simeq 30 \text{ GHz}$) and $\Delta u_{\text{fwhm}}/2 \simeq 77$ for the AMiBA ($D = 60 \text{ cm}$, $\nu_0 = 95 \text{ GHz}$; Fig. 1b). We can set a similar limit for the real-space pixel size, i.e., $\Delta \theta_p \lesssim \Delta \theta_{\text{fwhm}}/2$.

4. Observational Strategies and Applications: CBI and AMiBA Examples

In this section we describe three observational strategies and give simulation examples for the CBI and the AMiBA. The forthcoming interim AMiBA is an interferometric array of 7 elements. The characteristics of the AMiBA is summarized in Figure 1. Previous theoretical works and simulations on the AMiBA project can be found in Ng (2001, 2002), Pen et al. (2002), and Park & Park (2002).

4.1. Single Pointing Observation

In CMB interferometric observation, the observational strategy depends on the characteristics of the interferometric array, especially on the dish configuration and on the primary beam size in the uv -plane. In the *single pointing* strategy, the array observes many points on the sky. This strategy is appropriate for the interferometer that has uniform uv -coverage and sufficiently small primary uv -beam size. This interferometer like DASI can cover a wide range of angular scales and resolve the structures in the CMB power spectrum. One can increase the signal-to-noise ratio of visibility and reduce the sample variance of the CMB fluctuations by increasing integration time per field (t_f) and the number of independent fields (n_f), respectively (see Halverson et al. 2002 for the recent results of the single pointing observation of DASI).

In Figure 2a we plot the CMB power spectra of temperature anisotropy measured from the CBI mock survey adopting the single pointing strategy ($n_f = 30$, $t_f = 72$ hours) with band power widths of $\Delta u = \Delta u_{\text{fwhm}}/2 = 36$ (filled circles) and 72 (open circles). We assume that 13 elemental apertures ($D = 90$ cm) are located on a platform with DASI configuration given by White et al. (1999b, Table 1). We also assume that CBI complex correlators ($T_{\text{sys}} = 30$ K) have 5 channels around 26 – 36 GHz. During the observation of a specified field, the platform does not change its parallactic angle so that all baseline vectors keep constant orientations relative to the field. To estimate band powers from the mock visibility samples, we used the quadratic estimator described in §3.1. At high $\ell \gtrsim 2,000$, where noise dominates, strong band power anti-correlations exist. We define the band power correlation by $M_{bb'}/\sqrt{M_{bb}M_{b'b'}}$, where $M_{bb'}$ is the inverse Fisher matrix element $(\mathbf{F}^{-1})_{bb'}$. Correlations between neighboring bands at lower $\ell \lesssim 2,000$ are from -57% to -35% for $\Delta u = 36$, while they are between -19% and -16% for $\Delta u = 72$.

We can reduce the correlations among the band power estimates by sampling the visibilities in the uv -plane in such a way that the uv -space is better covered both in radial and transverse directions and the window functions of various baselines are densely overlapping. As a result of this, the resolution of the power spectrum in the ℓ -space (hereafter $\Delta\ell$ -resolution) can be increased. To demonstrate this idea, we consider a case with the CBI array whose platform rotates by 60° with steps of 10° , 6° , and 2° during the observation of a single field to get visibility samples with 6, 10, and 30 different orientations, respectively. These situations are very similar to the CBI deep fields case (Mason et al. 2002). Furthermore, the visibility data set with 6 orientations approximately equals to the data set in each pointing in the recent CBI mosaic observation (Pearson et al. 2002) that has 78 baselines, 10 channels, and 42 mosaic pointings. Here the total number of visibilities is $N_v \approx 200,000$, and the effective number of orientations is $200,000/780/42 \simeq 6$. We pixelize the uv -plane with $\Delta u_{\text{pix}} = 12$, and use equations (26) and (27) to reduce the data size. Figure 2b shows the power spectra measured from the pixelized CBI mock visibilities with 6 ($n_f = 15$, $t_f = 24^{\text{h}} \times 6$; open triangles), 10 ($n_f = 9$, $t_f = 24^{\text{h}} \times 10$; filled circles), and 30 ($n_f = 6$, $t_f = 12^{\text{h}} \times 30$; open circles) orientations. The anti-correlations between the power estimates at $\ell < 2,000$ are significantly reduced as the number of orientations increases. Table 2 summarizes the band power correlations and the band power uncertainties in the power estimations of the above four cases.

To further investigate the above method of increasing $\Delta\ell$ -resolution via the *uv-mosaicking*, we have simulated mock observations using a two-element interferometer with $D = 20$ cm ($\Delta u_{\text{fwhm}} = 51.2$) and two frequency channels (20 GHz whole bandwidth centered at $\nu_0 = 95$ GHz). The dishes change their separation from 40 cm to 60 cm, during which the platform is rotated to obtain nearly uniform visibility samples. We adopt different noise levels depending on the amplitudes of the model power spectrum, i.e., $\sigma_b = 43(C_\ell/C_{600})^{1/2}$ mJy per visibility. Figure 3 shows the distribution of visibilities in the *uv*-plane (upper right box) and the band powers estimated from 30 mock observations. The band width of the intermediate five bands is $\Delta u = 21$ ($\Delta\ell = 132$), and the band power correlations are between -29% and -18% , with an average of -24% .

Hobson & Maguiejo (1996) and Tegmark (1997c) derived useful formulae for the uncertainties of the measured power spectrum. Suppose that $\bar{S}(u_b)$ denotes the power $S(u)$ averaged over a band ranging from u_{b1} to u_{b2} centered on u_b . The rms error for this band power is given by $\sqrt{2}(\bar{S}(u_b) + \bar{S}^{\text{noise}}(u_b))$, where the first part is due to the sample variance, and the second is due to the noise variance. If there are $N(u_b)$ independent eigenmodes in a band and if n_f independent fields are observed, the error will drop by a factor of $\sqrt{n_f N(u_b)}$.

Let us grid the *uv*-plane with cell size u_0 . In the single pointing strategy, the natural choice for the cell size is $u_0 \simeq 1/\sqrt{\Omega_s}$ where Ω_s is the solid angle of the primary beam. Then, the noise power per *uv*-cell is given by

$$\sigma_N^2 = \frac{s^2 \Omega_s^2}{n_{\text{vis}} t_f} = \frac{s^2 \Omega_s^3}{\rho_{\text{vis}} t_f}, \quad (29)$$

where s is the sensitivity of the instrument in units of $\mu\text{K sec}^{1/2}$ given by $s = (\partial B_\nu / \partial T)^{-1} s_b / \Omega_s$, n_{vis} is the number of visibilities per *uv*-cell, and ρ_{vis} is the number of visibilities per unit area in the *uv*-plane; $n_{\text{vis}} = \rho_{\text{vis}} u_0^2$. Suppose that the sampled area in the half of the *uv*-plane is $A_0 = \pi(u_{b2}^2 - u_{b1}^2)/2$, and N_v is the number of visibilities in this area ($N_v = A_0 \rho_{\text{vis}}$). Given the detector sensitivity s , *uv*-plane coverage A_0 , and total observation time t_{tot} , we can specify a quantity to keep constant,

$$w^{-1} = \frac{s^2 A_0}{t_{\text{tot}}} = \frac{\sigma_N^2 N_v}{\Omega_s^3 n_f}, \quad (30)$$

where w can be considered as the noise weight per unit *uv*-area, and $t_{\text{tot}} = n_f t_f$.

From equations (29) and (30) the noise power spectrum can be obtained, $\bar{S}^{\text{noise}}(u_b) \simeq \sigma_N^2 u_0^2 = w^{-1} n_f \Omega_s^2 / N_v$. If $A_{\text{eff}}(u_b)$ is the effective area occupied by N_v^i independent visibility components, then $N(u_b) \approx N_v^i = A_{\text{eff}}(u_b) \Omega_s$ for sufficiently wide band. Therefore, the uncertainty limit for the band power estimation becomes

$$\Delta \bar{S}(u_b) \approx \sqrt{\frac{2}{n_f A_{\text{eff}}(u_b) \Omega_s}} \left(\bar{S}(u_b) + \frac{w^{-1} n_f \Omega_s^2}{N_v} \right). \quad (31)$$

How many pointings do we need to make to minimize the band power uncertainty? With t_{tot} and

Ω_s fixed, we minimize $\Delta\bar{S}(u_b)$ with respect to n_f to get the best choice

$$n_f = \frac{wN_v\bar{S}(u_b)}{\Omega_s^2} = \frac{t_{\text{tot}}N_v\bar{S}(u_b)}{s^2A_0\Omega_s^2}. \quad (32)$$

If n_f is fixed instead, the optimal observation time for each pointing becomes $t_f = s^2A_0\Omega_s^2/N_v\bar{S}(u_b)$. This corresponds to the limit making the noise and the sample variance contributions equal.

Let us consider an example using a two-element AMiBA with a single frequency channel ($N_v = N_v^i = 1$). We measure only one E -mode band power with a wide band centered at $u_b \simeq 206$, with $u_{b_1} \simeq 129$ and $u_{b_2} \simeq 283$, given by the FWHM limit of the uv -beam pattern (Eq. 28). The fluctuation power of E -polarization is expected to be $C_b^{EE} \approx 20 \mu\text{K}^2$ in our ΛCDM model. With $t_{\text{tot}} = 6$ months, we obtain the optimal parameters, $n_f = 32$ and $t_f = 135$ hours, which give the band power uncertainty $\Delta C_b \equiv 2\pi u_b^2 \Delta\bar{S}(u_b) \simeq 10 \mu\text{K}^2$. Our mock observations with these parameters has confirmed the validity of equation (31).

The time required for a 4σ detection of the CMB polarization using the AMiBA with 7 dishes is worth discussing. Unless we increase the number of independent modes $N(u_b)$ within the band, it would be impossible to get the 4σ limit by observing only one field even with infinite integration time due to the sample variance. Here we consider only the shortest baseline components ($N_v = 12$, $N_v^i = 3$). From equation (31) with a condition $\Delta\bar{S}(u_b) = \bar{S}(u_b)/4$, a 4σ detection of the E -polarization can be achieved in a minimum total observation time of $t_{\text{tot}} = 20$ days when $n_f = 43$.

4.2. Mosaicking

The resolution in the uv -space is limited by the area of the sky that is surveyed, which is equal to the size of the primary beam in a single pointing observation. By *mosaicking* several contiguous pointing observations, we can increase $\Delta\ell$ -resolution in the band power estimates. Mosaicking does not increase the u -range, but simply enhances the resolution by allowing us to follow more periods of a given wave (see W99 for a complete discussion). For close-packed interferometers such as the AMiBA and the CBI whose uv -beam size larger than the structure of the CMB power spectrum, mosaicking is essential to increase the $\Delta\ell$ -resolution. In particular, since the 7-element AMiBA has baselines of only three different lengths (see Fig. 1c), the uv -coverage is so sparse that the band powers estimated from a single pointing observation will have large sample variances and strong anti-correlations (Ng 2001).

The increase of $\Delta\ell$ -resolution by mosaicking can be demonstrated by using the effective uv -beam pattern

$$\tilde{A}_{\text{eff}}(\mathbf{u}, \nu) \equiv \frac{1}{N_{\text{mo}}} \sum_{i=1}^{N_{\text{mo}}} \tilde{A}_{\mathbf{y}_i}(\mathbf{u}, \nu) = \frac{1}{N_{\text{mo}}} \sum_{i=1}^{N_{\text{mo}}} \tilde{A}(\mathbf{u}, \nu) e^{i2\pi\mathbf{u}\cdot\mathbf{y}_i}, \quad (33)$$

where N_{mo} is the total number of contiguous pointings and \mathbf{y}_i is the i th pointing position on the sky. Figure 4 shows the profiles of the effective uv -beams resulted from 7- and 19-pointing mosaics

with separation $\delta\theta_{\text{mo}}$ in a hexagonal configuration. As the separation $\delta\theta_{\text{mo}}$ increases, the effective width becomes narrower. However, for $\delta\theta_{\text{mo}} > 20'$, complex correlations among the band power estimates are expected due to the sidelobe effects (e.g., see the long dashed curve in Fig. 4b). Figure 5 shows an example of the CMB temperature and polarization power spectra estimates expected in the AMiBA 19-pointing hexagonal mosaic mock observation in a period of 6 months. Using the AMiBA configured as in the Figure 1, we have made 10 independent mosaics with $\delta\theta_{\text{mo}} = 15'$ and an integration time of 22.7 hours per pointing ($n_f = 10$, $t_f = 22.7 \times 19$). The quadratic estimator and the optimal subspace filtering are applied to estimate the band powers with $\Delta u = 90$ (see §3.1). The band power window functions and the corresponding band power expectation values $\langle \mathcal{C}_b \rangle$ calculated from equations (16) and (17) are also shown. It shows that the measured band powers excellently match with the theoretical values.

For the mosaicking strategy, the uncertainty limit of the band power estimation in equation (31) is modified to

$$\Delta \bar{S}(u_b) \approx \sqrt{\frac{2}{n_f A_{\text{eff}}(u_b) \Omega_{\text{mo}}}} \left(\bar{S}(u_b) + \frac{w^{-1} n_f \Omega_s \Omega_{\text{mo}}}{N_v} \right), \quad (34)$$

where Ω_{mo} is the mosaicked area of each field. Here we have adopted a new uv -pixel size $u_0^2 \simeq 1/\Omega_{\text{mo}}$, and a new noise power per uv -cell $\sigma_N^2 = s^2 \Omega_s \Omega_{\text{mo}} / n_{\text{vis}} t_f$. The optimal mosaicked area can be obtained by minimizing $\Delta \bar{S}(u_b)$ with respect to Ω_{mo} , giving the condition, $\bar{S}(u_b) = w^{-1} n_f \Omega_s \Omega_{\text{mo}} / N_v$. Given a total observation time $t_{\text{tot}} = n_f t_f$, the best choice for the mosaicked area becomes

$$\Omega_{\text{mo}} = \frac{w N_v}{n_f \Omega_s} \bar{S}(u_b) = \frac{t_f N_v}{s^2 A_0 \Omega_s} \bar{S}(u_b). \quad (35)$$

As an example, let us consider the visibilities measured by the shortest baselines in the AMiBA polarization observation, as described in §4.1. With 7 dishes, the total number of visibility outputs is $N_v = 12$ with 3 independent baselines ($N_v^i = 3$), and the number of independent modes within the wide band ($u_b \simeq 206$, $u \simeq 129 - 283$) becomes $N(u_b) \approx N_v^i (\Omega_{\text{mo}} / \Omega_s) = A_{\text{eff}}(u_b) \Omega_{\text{mo}}$. From equation (35), we obtain an optimal square-shaped mosaic with size of θ_{opt} , assuming a total observation time $t_{\text{tot}} = 6$ months,

$$\theta_{\text{opt}} = \Omega_{\text{mo}}^{1/2} \approx \frac{7^\circ}{\sqrt{n_f}}. \quad (36)$$

Hence, from equations (34)–(36), the uncertainty of the band power estimate only depends on the total survey area $n_f \Omega_{\text{mo}}$ for a given total observation time t_{tot} , and is expected to be $\Delta \mathcal{C}_b \approx 2 \mu\text{K}^2$ for $t_{\text{tot}} = 6$ months. Note that choosing a smaller band width will increase $\Delta \mathcal{C}_b$; if there are n_b subbands within a certain wide band, the size of error bar for each subband in the wide band would be roughly $\Delta \mathcal{C}_b n_b^{1/2}$. Increasing Ω_{mo} (or decreasing n_f) will give better results since we can get more information from larger scales and hence increase the resolution of the band power width $\Delta \ell \gtrsim \pi / \theta_{\text{opt}}$. Table 3 summarizes the optimal parameter choices for the single pointing and mosaicking strategies, given a total observation time $t_{\text{tot}} = 6$ months.

Figures 6a, 6b, and 6c show the CMB power spectra expected in an AMiBA experiment when it performs 12×12 mosaic ($\delta\theta_{\text{mo}} = 15'$) observations of $3^\circ \times 3^\circ$ area over five fields ($n_f = 5$) with 6 hours of integration time per pointing. We have assumed two frequency channels and used the quadratic estimator as well as the signal-to-noise eigenmode analysis in our computation. Except for the first and the last bands, the band power width is chosen to be $\Delta u = 45$ ($\Delta\ell = 283$). The ℓ -location of each band power is roughly estimated from the noise-weighted window function defined as

$$W_\ell^N / \ell \equiv \text{Tr} \left[\mathbf{N}^{-1/2} \frac{\partial \mathbf{S}}{\partial \mathcal{C}_\ell} \mathbf{N}^{-1/2} \right] / N_\ell, \quad (37)$$

where the prewhitening transformation in §3.1 is applied, and N_ℓ is the number of data points that contribute to the sensitivity at ℓ (Bond et al. 1998). Note that equation (37) is an approximate window function, and the Fisher matrix-derived window function (Eq. 17) should be used in general. The band power correlations are sufficiently small with the average of about -10% . We have made two sets of measurement of the band powers with band centers shifted by the half of the band width with respect to each other. The Λ CDM model power spectra convolved with a box of band power width weighted by the window function in equation (37) are plotted to guide comparison between the measured powers and the theory (thin curves and squares). Since there are about 4 bands ($n_b \approx 4$) within the range of a wide band in this case ($u \simeq 129 - 283$ centered at $u_b \simeq 206$), one would expect the estimated E -polarization band powers near $u_b = 206$ to be $\sigma(\mathcal{C}_b) \approx \Delta \mathcal{C}_b n_b^{1/2} \approx 4 \mu\text{K}^2$, which coincides with the uncertainty of the fourth band power in Figure 6b ($4.1 \mu\text{K}^2$) and validates equation (34).

4.3. Drift-Scanning

In the mosaic strategy, one has to track every pointing of a specified mosaic field for a sufficiently long time. This inevitably suffers from severe ground pickups since the ground emission usually changes abruptly as the platform of the array turns around during its tracking. *Drift-scanning* is the simplest way to remove the ground contamination because an interferometer is insensitive to the ground emission that is a DC signal (Pen et al. 2002). In this strategy the direction of the array is fixed while the sky drifts along the constant declination as the earth rotates. After some time, the array slews to the original starting position, and observes the sky along the same scanning path. In the drift-scan mode, the visibility is a function of time along a scan path.

To estimate the power spectrum by using reasonable computer resources, the time-ordered visibility samples must be compressed (see §3.2). During the compression, the data experiences effects of smoothing over the pixel scale. If we consider only the real-space pixelization, a pixelized visibility $V_{\mathbf{y}_p}^T(\mathbf{u}_k)$ is related with the time-ordered visibilities $V_{\mathbf{y}(t)}^T(\mathbf{u}_k)$ by

$$V_{\mathbf{y}_p}^T(\mathbf{u}_k) = \int d^2y W_p(\mathbf{y} - \mathbf{y}_p) V_{\mathbf{y}(t)}^T(\mathbf{u}_k)$$

$$\begin{aligned}
&= \frac{\partial B_\nu}{\partial T} \int d^2 y W_p(\mathbf{y} - \mathbf{y}_p) \int d^2 v \tilde{A}(\mathbf{v}) e^{i2\pi \mathbf{v} \cdot \mathbf{y}} \Delta \tilde{T}(\mathbf{u}_k - \mathbf{v}) \\
&= \frac{\partial B_\nu}{\partial T} \int d^2 v \tilde{A}(\mathbf{v}) \tilde{W}_p(\mathbf{v}) e^{i2\pi \mathbf{v} \cdot \mathbf{y}_p} \Delta \tilde{T}(\mathbf{u}_k - \mathbf{v}),
\end{aligned} \tag{38}$$

where $\tilde{W}_p(\mathbf{v})$ is the Fourier transform of the smoothing filter $W_p(\mathbf{y})$, $\mathbf{y} = \mathbf{y}(t)$ is the drift-scan path, and \mathbf{y}_p denotes the real-space pixel position on the sky.

We have made an idealized mock AMiBA experiment in which the array drift-scans a small square field of $2^\circ \times 2^\circ$ size near the celestial equator (for flat sky approximation). The platform does not change its parallactic angle during the observation. This enables us to consider only the real-space pixelization in the data compression. After scanning a 2° path, the next path $10'$ apart from the previous one is scanned. The T , Q , and U visibilities are functions of time determined by the rotating speed of the sky, and are accumulated every 8 seconds. Also, according to equation (36), the AMiBA drift-scans a square field of $2^\circ \times 2^\circ$ many times in a way described above for $t_f = 15$ days, and finally observes totally $n_f = 12$ independent fields in 6 months. The time-ordered visibility samples are then compressed as described in §3.2 to the pixelized visibility data set with 12×12 mosaic format and with $10'$ pixel size. The pixel smoothing effect is significant only in the scan direction. In this situation $\tilde{W}_p(\mathbf{v})$ in equation (38) is top-hat smoothing filter

$$\tilde{W}_p(v_x) = \frac{\sin(\pi v_x \Delta \theta_p)}{\pi v_x \Delta \theta_p}, \tag{39}$$

where $\Delta \theta_p = 10'$ is the real-space pixel size used in the data compression, and x denotes the scan direction. The visibility covariance matrix for the top-hat filtered drift-scan samples is obtained by modifying equations (6) and (7),

$$M_{mn}^{ij} = \frac{\partial B_{\nu_i}}{\partial T} \frac{\partial B_{\nu_j}}{\partial T} \int d^2 w \tilde{A}_{\mathbf{y}_m}(\mathbf{u}_i - \mathbf{w}, \nu_i) \tilde{A}_{\mathbf{y}_n}^*(\mathbf{u}_j - \mathbf{w}, \nu_j) \tilde{W}_p(u_{ix} - w_x) \tilde{W}_p(u_{jx} - w_x) \mathcal{S}_{XY}(\mathbf{w}), \tag{40}$$

and likewise for N_{mn}^{ij} . The band power estimates from the visibilities obtained by the mock drift-scanning are shown in Figures 6d, 6e and 6f, with a band width $\Delta u = 62.5$ except for the first and the last bands. The band power correlations between neighboring bands are from -12% to -10% .

5. Fast Unbiased Estimator

The AMiBA is expected to observe the sky over 100 deg^2 with the drift-scanning strategy. Even if the pixelization is applied to compress the time-ordered visibility samples, it is still a formidable task for a data pipeline using the maximum likelihood quadratic estimator to compute the power spectra. In this section we propose a fast power spectrum estimator that can be implemented without recourse to large computing resource. The basic idea comes from the correlation function analysis, first developed by Szapudi et al. (2001), and from the MASTER method of Hivon et al. (2002). The visibilities are, by definition, the beam-convolved CMB Fourier modes (e.g.,

$V^T(\mathbf{u}) \propto \int d^2v \tilde{A}(\mathbf{v}) \Delta \tilde{T}(\mathbf{u} - \mathbf{v})$. Therefore, the correlation between a pair of visibilities are directly related with the power spectrum (Eqs. 6 and 7). We introduce an approximate expression,

$$V_i V_j - N_{ij} \approx S_{ij} = \sum_b B_{ij}(b) \mathcal{C}_b, \quad (41)$$

where $B_{ij}(b) \equiv \partial S_{ij} / \partial \mathcal{C}_b$ ($i, j = 1, 2, \dots, N_p$; $b = 1, 2, \dots, N_b$). The ensemble average of the above equation restores equation (11), $\langle V_i V_j \rangle = S_{ij} + N_{ij}$.

First, we perform the whitening transformation of the noise covariance matrix \mathbf{N} , the instrument filter function $B_{ij}(b)$, and the visibility data vector \mathbf{V} as shown in equation (18). Since \mathbf{N} is assumed to be diagonal, the transformed quantities are δ_{ij} , $B_{ij}/\sigma_i \sigma_j$ ($\equiv B_{ij}^w$), and V_i/σ_i ($\equiv V_i^w$), respectively. Equation (41) then becomes

$$V_i^w V_j^w - \delta_{ij} = \sum_b B_{ij}^w(b) \mathcal{C}_b. \quad (42)$$

For a given band, complex pair weighting might be required for each ij -pair because of the uneven uv -coverage. However, we adopt an uniform weighting scheme with equal weights.

After a careful rearrangement of all components of $V_i^w V_j^w - \delta_{ij}$, $B_{ij}^w(b)$, and \mathcal{C}_b into simpler forms, $\{v_k\}$, $\{\beta_{kb}\}$, and $\{c_b\}$, respectively, by merging an ij -pair to an index k , we can rewrite equation (42) as $\mathbf{v} = \boldsymbol{\beta} \mathbf{c}$. The fast unbiased estimator (FUE) of the CMB power spectrum is obtained as

$$\mathbf{c} = [\boldsymbol{\beta}^T \boldsymbol{\beta}]^{-1} \boldsymbol{\beta}^T \mathbf{v}, \quad (43)$$

where

$$(\boldsymbol{\beta}^T \boldsymbol{\beta})_{bb'} = \sum_{i,j} B_{ij}^w(b) B_{ij}^w(b'), \quad (44)$$

and

$$(\boldsymbol{\beta}^T \mathbf{v})_b = \sum_{i,j} B_{ij}^w(b) (V_i^w V_j^w - \delta_{ij}). \quad (45)$$

The computation of equations (44) and (45), which are $\mathcal{O}(N_p^2)$ operations, is straightforward without need of any large memory and disk space. The FUE method is fast especially when the noise covariance matrix \mathbf{N} is diagonal. Even for the non-diagonal noise covariance matrix, however, the FUE is still fast since the prewhitening transformation is required just once. If the visibility samples are sufficiently separated so that they are considered as almost independent, the signal covariance matrix \mathbf{S} (also $B_{ij}(b)$) can be approximated to be diagonal. This approach, which is very similar to a multi-band generalization of the Boughn-Cottingham statistic (Boughn et al. 1992), can accelerate the FUE speed from $\mathcal{O}(N_p^2)$ to $\mathcal{O}(N_p)$ operations.

To constrain cosmological models using the FUE estimated power spectrum, we need to know the uncertainty for each \mathcal{C}_b and the covariance between the band powers or the band power window functions. The uncertainty of each band power estimated by FUE can be obtained by a Monte Carlo simulation (see, e.g., Hivon et al. 2002). By fitting or interpolating the band power estimates

$\{\mathcal{C}_b\}$, we can obtain a smooth CMB power spectrum $\mathcal{C}_\ell^{\text{fit}}$, from which many mock observations are made by including CMB signals, instrumental noises, and other characteristics of the experiment. The mock data sets are analyzed in the same way as the real data, giving rise to a set of power spectrum estimates $\{\{\mathcal{C}_b^{\text{m1}}\}, \{\mathcal{C}_b^{\text{m2}}\}, \dots\}$. The covariance matrix of the band powers

$$C_{bb'} \equiv \left\langle \left(\mathcal{C}_b^{\text{fit}} - \langle \mathcal{C}_b^{\text{m}} \rangle_{\text{mock}} \right) \left(\mathcal{C}_{b'}^{\text{fit}} - \langle \mathcal{C}_{b'}^{\text{m}} \rangle_{\text{mock}} \right) \right\rangle_{\text{mock}}, \quad (46)$$

is calculated. The uncertainty for each band power \mathcal{C}_b is then given by the square root of the diagonal components of \mathbf{C} , i.e., $\Delta\mathcal{C}_b = C_{bb}^{1/2}$.

We apply the FUE method to the AMiBA 19-pointing mosaic data to measure the band powers $\{\mathcal{C}_b\}$ with error bars estimated from 30 simulation data sets (open stars in Fig. 5). The band power estimates by FUE are quite consistent with those obtained by the quadratic estimator. However, most of the FUE error bars are bigger than those of the quadratic estimator. Note that the FUE is a sub-optimal quadratic estimator with \mathbf{N}^{-1} compared to $(\mathbf{S} + \mathbf{N})^{-1}$ of the optimal quadratic estimator.

6. Discussion

We have simulated interferometric observation of CMB temperature and polarization fluctuations. For each observational strategy the data pipelines from the time-ordered raw visibility samples to the CMB angular power spectra (\mathcal{C}_b^{TT} , \mathcal{C}_b^{EE} , and \mathcal{C}_b^{TE}) have been developed. The pipelines are composed of making mock observation, data compression, and power spectrum estimation. Data compression is achieved by pixelization of time-ordered visibilities in real- and uv -spaces by means of a common map-making process. This method can be applied to any kind of interferometric observation (see §3.2). In estimating the band powers from the mock visibility samples, the optimal subspace filtering or signal-to-noise eigenmode analysis along with the quadratic estimator was used. By discarding the modes with low signal-to-noise ratios, we were able to reduce the data set to a manageable size. One drawback of the optimal subspace filtering is that while it conserves the information with signal-to-noise ratio higher than the limit of eigenvalue threshold, some useful information may be lost in certain cases. For instance, in measuring the CMB polarization power spectrum, if the band width is too small to keep sufficient amount of the signal compared with the noise level, the weak signal can disappear during the optimal subspace filtering. Therefore, we need to choose a wider band width to obtain a higher signal-to-noise ratio, especially at higher ℓ region.

The measured band powers are found to be quite consistent with the band power expectation values $\langle \mathcal{C}_b \rangle$ for the AMiBA 19-pointing mosaic (Fig. 5). This implies that our data pipelines are working reliably. Using the fact that the visibility contains direct information of CMB power spectrum, we have developed a fast unbiased estimator of the CMB power spectra (FUE, §5) that requires only $\mathcal{O}(N_p^2)$ operations. This method is very similar to the power spectrum estimation method using Gabor transform (Hansen, Górski, & Hivon 2002). The FUE also gives band power

estimates that are consistent with those from the quadratic estimator (see Fig. 5). The FUE method does not require large computer resources. Given the precomputed quantities $B_{ij}(b) = \partial S_{ij} / \partial \mathcal{C}_b$, the computational speed is extremely fast. Even if the noise covariance matrix is highly non-diagonal, which is the usual case in real data analyses (e.g., handling constraint matrices to subtract the point source effect), the FUE method is still fast because the prewhitening transformation of $B_{ij}(b)$ and V_i is needed only once.

Our main goal was to propose data analysis techniques for each observational strategy of a CMB interferometer, especially when the uv -beam size is larger than the scale of structures in the CMB power spectrum. Using the mock CBI single pointing observations, we have investigated the effect of rotation of the array platform on the band power correlations and the uncertainties of the band powers. Based on the results, summarized in Figure 2 and Table 2, we conclude that the band power anti-correlations can be reduced by rotating the platform and thus densely sampling the visibility plane. However, the uncertainties of the band power estimates slightly increase (when the total integration time is fixed). This is because the CMB signal is shared by the neighboring visibilities due to the finite beam size. In this way, we can increase the resolution of the power spectrum in the ℓ -space down to a resolution limit $\Delta\ell \approx \pi/\theta$ given by the sampling theorem.

Using the recent CBI result of single pointing observation, Mason et al. (2002) have shown a power spectrum with band width of $\Delta\ell = 4\sqrt{2} \ln 2 / \theta_{\text{fwhm}} \approx 300$. This limit for $\Delta\ell$ is the FWHM of the visibility window function, which is proportional to the square of the Fourier transform of the primary beam with θ_{fwhm} (Pearson et al. 2002). On the other hand, our choice for the band width is $\Delta\ell = 226$ ($\Delta u = \Delta u_{\text{fwhm}}/2 = 36$). This is the limit given by the sampling theorem ($\Delta\ell \approx \pi/\theta$). It is $\Delta\ell = 4 \ln 2 / \theta_{\text{fwhm}}$ for a Gaussian primary beam, which is a factor of $\sqrt{2}$ narrower than that adopted by CBI team. We show in Table 2 that a mock CBI observation with 30 different orientations results in about 20% anti-correlations between neighboring bands at $\ell \lesssim 1,000$, and higher values at higher $\ell \gtrsim 1,000$, while they are 10 – 15% in Mason et al. (2002) due to the wider band width. The band power correlation at high ℓ regions can be reduced by more densely sampling visibilities with sufficient integration time. As shown in the example of uv -mosaicking using a two-element interferometer (Fig. 3), the band widths of power spectrum can be reduced while keeping the band correlations at a tolerable level by increasing the number of rotation steps with increasing dish separation, and by assigning longer integration time to the visibilities at low CMB signal regions. For intermediate five bands, the band width and the average band power correlation are $\Delta\ell = 132$ ($\Delta u = 21$) and -24% , respectively. The width is smaller than our resolution limit ($\Delta\ell = 161$, $\Delta u = \Delta u_{\text{fwhm}}/2$ where $\Delta u_{\text{fwhm}} = 51.2$), also a factor of 1.7 narrower than the limit obtained by Pearson et al.’s formula ($\Delta\ell \simeq 230$).

The recent DASI power spectrum is measured from the single pointing observation without platform rotation (Halverson et al. 2002). The DASI band powers have the resolution of $\Delta\ell \approx 80$ (with 18 – 28% anti-correlations), which is broader than the resolution limit $\Delta\ell = 4\sqrt{2} \ln 2 / \theta_{\text{fwhm}} = 66$ where $\theta_{\text{fwhm}} = 3^\circ.4$. We expect that the DASI single pointing observation with dense rotation of platform will allow higher resolution of about $\Delta\ell = 50$ at the similar level of anti-correlations. Since

the mosaicking is the most efficient method for increasing the resolution of the power spectrum, the combination of mosaicking and dense rotation of the platform followed by the uv -pixelization is thought to be the most ideal observational strategy for DASI- and CBI-type CMB interferometers.

For each observational strategy, optimal parameter choices for the AMiBA experiment are discussed in §4, and summarized in Table 3. The 7-element AMiBA is expected to detect CMB polarization power spectrum near $\ell \approx 1,300$ at 4σ level within 20 days by observing 43 fields. In AMiBA mosaicking with $t_{\text{tot}} = 6$ months, the optimal parameter sets are ($\theta_{\text{opt}} = 7^\circ$, $n_f = 1$) or ($\theta_{\text{opt}} = 3^\circ$, $n_f = 5$) for a minimum uncertainty of the E -polarization power spectrum. In fact, the optimal parameters strongly depend on the characteristics of the interferometer (e.g., η_s , η_a , and T_{sys}) and on the E -polarization power spectrum C_b^{EE} . Since we are considering the shortest baselines in deriving the parameters, the optimization is only for the sensitivity range of the shortest baselines ($\ell < 2,000$). At higher ℓ -range ($\ell > 2,000$) where the 7-element AMiBA has only a few baselines, the CMB polarized signal is expected to be very low. Therefore, we have chosen a wider band width for the last band for the 12×12 mosaicking and drift-scanning observations (see Fig. 6). To obtain a meaningful polarization power spectrum at high ℓ region with narrow band widths, we need to increase the integration time or the number of baselines. This can be seen in the simulation of the 19-pointing mosaicking by AMiBA where the integration time per pointing is almost one day (see Fig. 5). Although the band widths are quite wide in the temperature power spectra in Figure 6, we can measure temperature band powers independently with narrower band width because the signal-to-noise ratios of the T visibilities are very high, compared with those of polarization ($\Delta\ell = 196$, see open circles in Fig. 6d).

Among the three observational strategies that we have studied, the single pointing is useful for a detection of the CMB polarized signal while the mosaicking or the drift-scanning of a large area of the sky is essential for measuring the polarization power spectrum with high $\Delta\ell$ -resolution. The drift-scanning strategy is efficient for removing the ground contamination. It can also save half of the integration time when compared to the method of differencing two fields in the removal of the ground spillover adopted by the CBI experiment (Padin et al. 2001). In the drift-scanning, the survey region can have a shape for which the flat-sky approximation is inapplicable. Since the survey area drift-scanned by the AMiBA interferometer will be over 100 deg^2 , it is necessary to take into account the curvature of the sky. Our future work will deal with important issues such as the removal of Galactic foreground emission, the identification of radio point sources, and the subtraction of unresolved point sources. It is also important to study the topology of the CMB temperature and polarization fields to test the primordial fluctuations for Gaussianity (see, e.g., Park & Park 2002).

We acknowledge valuable discussions with J.-H. Protty Wu, Ue-Li Pen, Tzihong Chiueh, Mike Kesteven, Cheng-Juin Ma, and helpful comments from the anonymous referee. CGP and CP were supported by the BK21 program of the Korean Government and the Basic Research Program of the Korea Science & Engineering Foundation (grant no. 1999-2-113-001-5). CGP acknowledges

helpful comments with Hyun Seok Yang, and the support by the CosPA Center at the National Taiwan University during his visit. KWN was supported in part by the National Science Council, Taiwan ROC under the Grant NSC90-2112-M-001-028.

Table 1. Ensemble Averages of the Conjugate Products of T , Q , and U Pairs in the uv -Plane.

XY	$\langle \tilde{X}(\mathbf{v})\tilde{Y}^*(\mathbf{w}) \rangle = \mathcal{S}_{XY}(\mathbf{w})\delta(\mathbf{v} - \mathbf{w})$
TT	$\mathcal{S}_{TT}(\mathbf{w}) = S_{TT}(w)$
TQ	$\mathcal{S}_{TQ}(\mathbf{w}) = S_{TE}(w) \cos 2\phi_{\mathbf{w}}$
TU	$\mathcal{S}_{TU}(\mathbf{w}) = S_{TE}(w) \sin 2\phi_{\mathbf{w}}$
QQ	$\mathcal{S}_{QQ}(\mathbf{w}) = S_{EE}(w) \cos^2 2\phi_{\mathbf{w}} + S_{BB}(w) \sin^2 2\phi_{\mathbf{w}}$
QU	$\mathcal{S}_{QU}(\mathbf{w}) = S_{EE}(w) \cos 2\phi_{\mathbf{w}} \sin 2\phi_{\mathbf{w}} - S_{BB}(w) \sin 2\phi_{\mathbf{w}} \cos 2\phi_{\mathbf{w}}$
UU	$\mathcal{S}_{UU}(\mathbf{w}) = S_{EE}(w) \sin^2 2\phi_{\mathbf{w}} + S_{BB}(w) \cos^2 2\phi_{\mathbf{w}}$

Table 2. Band Power Correlations $M_{bb'}/\sqrt{M_{bb}M_{b'b'}}$ and Relative Uncertainties $\Delta\mathcal{C}_b/\mathcal{C}_b$ in the Mock CBI Observations^a

n_f	t_f	$M_{bb'}/\sqrt{M_{bb}M_{b'b'}}^b$							Average	
		(b, b')	(1, 2)	(2, 3)	(3, 4)	(4, 5)	(5, 6)	(6, 7)		
30	72 ^h		−0.35	−0.34	−0.34	−0.43	−0.48	−0.57	...	−0.41
15	24 ^h × 6 ^{ori.}		−0.25	−0.29	−0.27	−0.40	−0.44	−0.43	...	−0.35
9	24 ^h × 10 ^{ori.}		−0.21	−0.23	−0.23	−0.33	−0.40	−0.44	...	−0.30
6	12 ^h × 30 ^{ori.}		−0.21	−0.21	−0.22	−0.31	−0.33	−0.36	...	−0.27
$\Delta\mathcal{C}_b/\mathcal{C}_b$										
n_f	t_f	b	1	2	3	4	5	6	7	Average
30	72 ^h		0.15	0.23	0.11	0.17	0.14	0.18	0.21	0.17
15	24 ^h × 6 ^{ori.}		0.15	0.27	0.14	0.17	0.20	0.18	0.19	0.19
9	24 ^h × 10 ^{ori.}		0.14	0.28	0.15	0.20	0.21	0.22	0.25	0.21
6	12 ^h × 30 ^{ori.}		0.13	0.33	0.20	0.23	0.24	0.22	0.25	0.23

^aThe total observation time is set to $t_{\text{tot}} = 90$ days.

^b $M_{bb'}$ is the inverse Fisher matrix element $(\mathbf{F}^{-1})_{bb'}$.

Note. — Only the first 7 band power estimates ($\Delta u = 36$ or $\Delta\ell = 226$) are considered.

Table 3. Optimal Parameters for AMiBA Single Pointing and Mosaicking Strategies^a

Single Pointing			
n_d^b	n_f	t_f	$\Delta\mathcal{C}_b^c$
2	32	135 hrs	10 μK^2
7	380	11.4 hrs	2 μK^2
Square Mosaicking ($n_d = 7$)			
θ_{opt}	n_f	t_f	$N_{\text{mo}} (\delta\theta_{\text{mo}} = 15')$
7°	1	180 days	28×28
3°	5	36 days	12×12

^aThe total observation time is set to $t_{\text{tot}} = 6$ months.

^bNumber of dishes.

^c E -mode band power uncertainty. The band width of the AMiBA shortest baselines is $\Delta u = 154$, centered at $u_b = 206$.

REFERENCES

- Bond, J.R., Jaffe, A.H., & Knox, L. 1998, *Phys. Rev. D*, 57, 2117
- Boughn, S.P., Cheng, E.S., Cottingham, D.A., & Fixsen, D.J. 1992, *ApJ*, 391, L49
- de Oliveira-Costa, A., Tegmark, M., Zaldarriaga, M., Barkats, D., Gundersen, J.O., Hedman, M.M., Staggs, S.T., & Winstein, B. 2002, preprint, astro-ph/0204021
- Halverson, N.W., et al. 2002, *ApJ*, 568, 38
- Hansen, F.K., Górski, K.M., & Hivon, E. 2002, *MNRAS*, 336, 1304
- Hedman, M.M., Barkats, D., Gundersen, J.O., McMahon, J.J., Staggs, S.T., & Winstein, B. 2002, *ApJ*, 573, L73
- Hedman, M.M., Barkats, D., Gundersen, J.O., Staggs, S.T., & Winstein, B. 2001, *ApJ*, 548, L111
- Hivon, E., Górski, K.M., Netterfield, C.B., Crill, B.P., Prunet, S., & Hansen, F. 2002, *ApJ*, 567, 2
- Hobson, M.P., Lasenby, A.N., & Jones, M. 1995, *MNRAS*, 275, 863
- Hobson, M.P., & Magueijo, J. 1996, *MNRAS*, 283, 1133
- Hobson, M.P., & Maisinger, K. 2002, *MNRAS*, 334, 569 (HM02)
- Hu, W., & White, M. 1997, *New Astronomy*, 2, 323
- Jaffe, A.H., et al. 2001, *Phys. Rev. Lett.*, 86, 3475
- Janssen, M.A., & Gulkis, S. 1992, in *The Infrared and Submillimeter Sky after COBE*, ed. M. Signore & C. Dupraz (Dordrecht: Kluwer), 391
- Keating, B.G., O'Dell, C.W., de Oliveira-Costa, A., Klawikowski, S., Stebor, N., Piccirillo, L., Tegmark, M., & Timbie, P.T. 2001, *ApJ*, 560, L1
- Knox, L. 1999, *Phys. Rev. D*, 60, 103516
- Kovac, J., Leitch, E.M., Pryke, C., Carlstrom, J.E., Halverson, N.W., & Holzappel, W.L. 2002, *Nature*, 420, 772
- Leitch, E.M., et al. 2002a, *ApJ*, 568, 28
- Leitch, E.M., et al. 2002b, *Nature*, 420, 763
- Lo, K.Y., Chiueh, T.H., Martin, R.N., Ng, K.-W., Liang, H., Pen, U.-L., & Ma, C.-P. 2001, in *New Cosmological Data and the Values of the Fundamental Parameters*, ed. A. Lasenby & A. Wilkinson, IAU Symp. 201 (San Francisco: ASP)

- Mason, B.S., et al. 2002, preprint, astro-ph/0205384
- Mather, J.C., Fixsen, D.J., Shafer, R.A., Mosier, C., & Wilkinson, D.T. 1999, ApJ, 512, 511
- Myers, S.T., et al. 2002, preprint, astro-ph/0205385
- Netterfield, C.B., Devlin, M.J., Jarolik, N., & Wollack, E.J. 1997, ApJ, 474, 47
- Ng, K.-W. 2001, Phys. Rev. D, 63, 123001
- Ng, K.-W. 2002, in AMiBA 2001: High-Z Clusters, Missing Baryons, and CMB Polarization, ed. L.W. Chen, C.-P. Ma, K.-W. Ng, and U.-L. Pen, ASP Conf. Ser. Vol. 257 (San Fransisco: ASP)
- O’Sullivan, C., et al. 1995, MNRAS, 274, 861
- Padin, S., et al. 2001, ApJ, 549, L1
- Park, C.-G., & Park, C. 2002, J. of Korean Astron. Soc., 35, 67
- Pearson, T.J., et al. 2002, preprint, astro-ph/0205388
- Pen, U.-L., Ng, K.-W., Kesteven, M.J., & Sault, B. 2002, preprint
- Pryke, C., Halverson, N.W., Leitch, E.M., Kovac, J., Carlstrom, J.E., Holzapel, W.L., & Dragovan, M. 2002, ApJ, 568, 46
- Scott, P.F., et al. 1996, ApJ, 461, L1
- Scott, P.F., et al. 2002, preprint, astro-ph/0205380
- Seljak, U. 1997, ApJ, 482, 6
- Seljak, U., & Zaldarriaga, M. 1996, ApJ, 469, 437
- Stompor, R., et al. 2002, Phys. Rev. D, 65, 22003
- Szapudi, I., Prunet, S., Pogosyan, D., Szalay, A.S., & Bond, J.R. 2001, ApJ, 548, L115
- Taylor, A.C., et al. 2002, preprint, astro-ph/0205381
- Tegmark, M. 1997a, ApJ, 480, L87
- Tegmark, M. 1997b, Phys. Rev. D, 55, 5895
- Tegmark, M. 1997c, Phys. Rev. D, 56, 4514
- Tegmark, M., & de Oliveira-Costa, A. 2001, Phys. Rev. D, 64, 63001
- Tegmark, M., Taylor, A.N., & Heavens, A.F. 1997, ApJ, 480, 22

- van Waerbeke, L. 2000, MNRAS, 313, 524
- White, M., Carlstrom, J.E., Dragovan, M., & Holzapfel, W.L. 1999a, ApJ, 514, 12 (W99)
- White, M., Carlstrom, J.E., Dragovan, M., & Holzapfel, W.L. 1999b, astro-ph/9912422
- Wrobel, J.M., & Walker, R.C. 1999, in Synthesis Imaging in Radio Astronomy II, ed. G.B. Taylor, C.L. Carilli, and R.A. Perley, ASP Conf. Ser. Vol. 180 (San Fransisco: ASP)
- Wu, J.-H.P. 1999, Ph.D. thesis, University of Cambridge, UK
- Wu, J.-H.P. 2002, private communication
- Zaldarriaga, M., & Seljak, U. 1997, Phys. Rev. D, 55, 1830
- Zaldarriaga, M., Seljak, U., & Bertschinger, E. 1998, ApJ, 494, 491

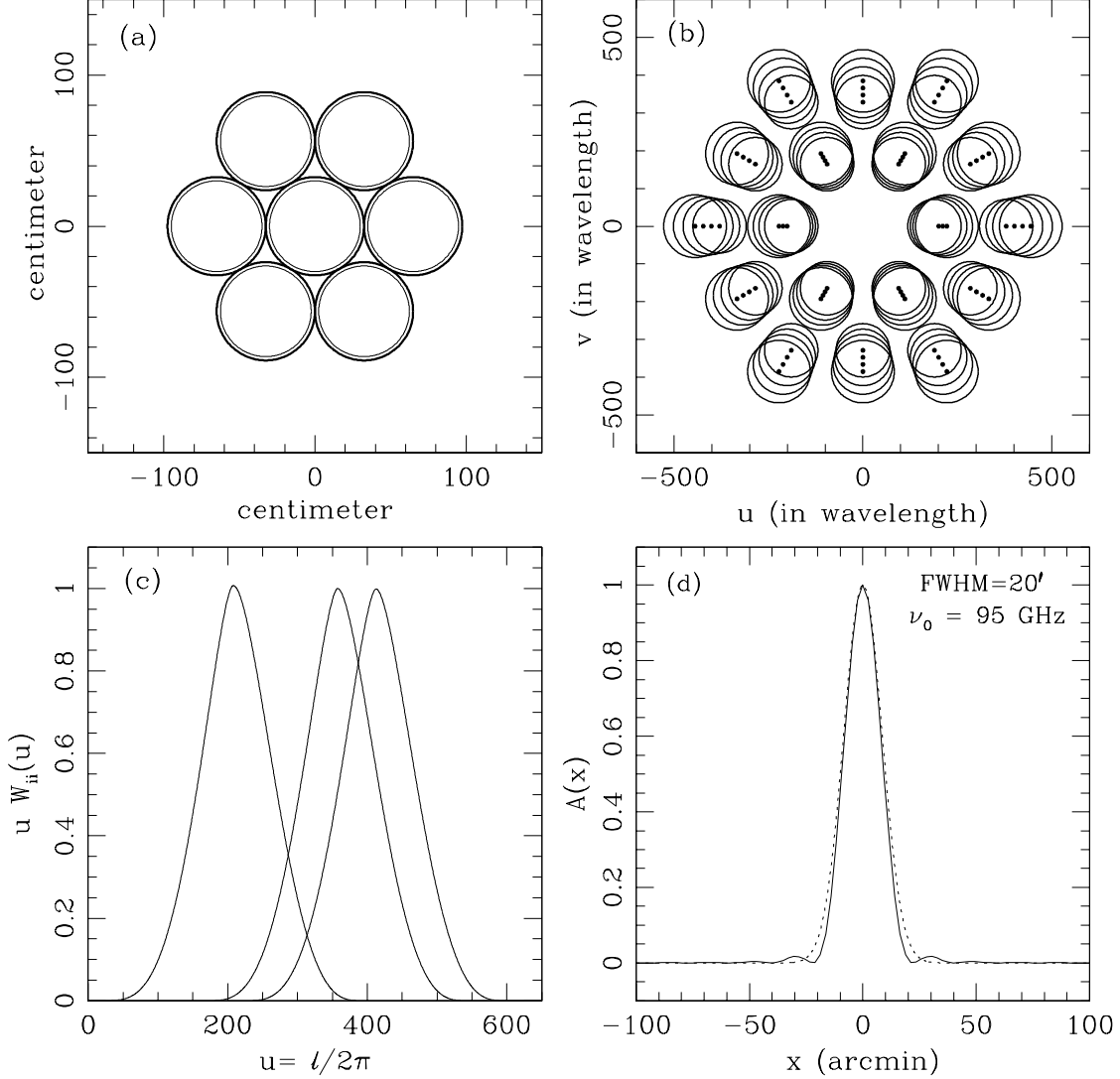


Fig. 1.— (a) Close-packed hexagonal configuration of seven receivers ($D = 60$ cm) of the AMiBA on a single platform. Each feed horn can detect T , Q , U , and V Stokes parameters simultaneously using complex dual polarizer with $T_{sys} = 70$ K. Thin circles are boundaries of the physical dishes, and the shields between the 5 cm gaps of the adjacent dishes are drawn as thick circles. Due to the hexagonal configuration, the instrument gives 21 baselines with 3 different lengths in different directions. (b) The uv -coverage for a snapshot of the sky with the configuration shown in (a). Four frequency channels are assumed ($\nu_0 = 95$ GHz, $\Delta\nu = 20$ GHz whole bandwidth). The points are the uv -coordinates of the baseline vectors, and the circles have diameters equal to the FWHM of the uv -beam pattern. (c) The sensitivity of AMiBA at the center frequency $\nu_0 = 95$ GHz shown by the window functions for the three baselines with different lengths (Eq. 14 of W99). (d) The real-space primary beam pattern $A(\mathbf{x})$ at the center frequency (solid curve), and a Gaussian function with FWHM $\simeq 20'$ (dotted curve) approximating the beam.

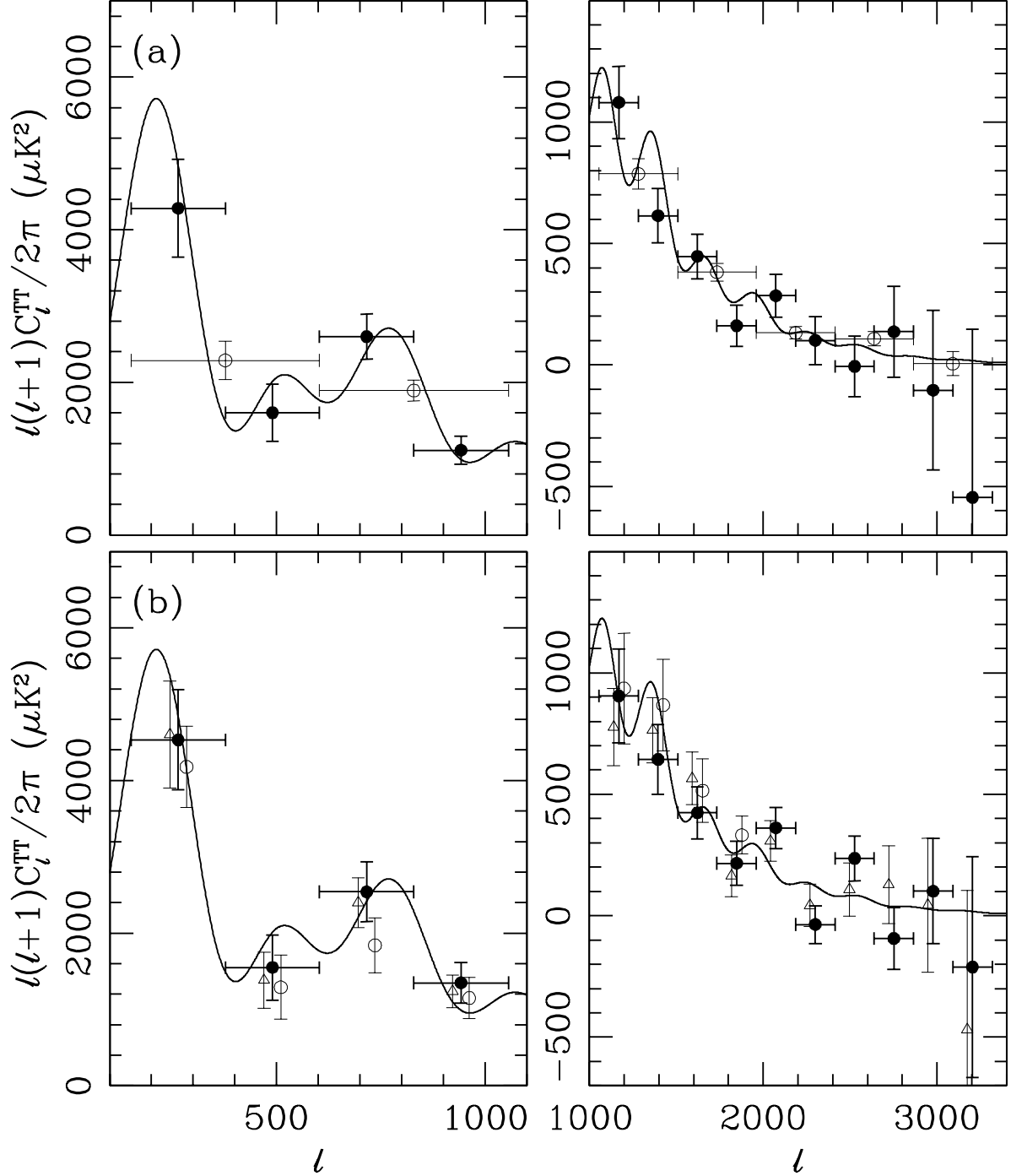


Fig. 2.— (a) The power spectra of the CMB temperature anisotropy measured from a mock CBI observation ($n_f = 30$, $t_f = 72^h$) with band power widths $\Delta u = 36$ (filled circles) and 72 (open circles). (b) Power spectra measured from mock CBI observations with 6 ($n_f = 15$, $t_f = 24^h \times 6$; open triangles), 10 ($n_f = 9$, $t_f = 24^h \times 10$; filled circles), and 30 ($n_f = 6$, $t_f = 12^h \times 30$; open circles) orientations. Each figure is divided into two panels at low and high ℓ regions. To avoid confusion, the open triangles and circles are slightly shifted to the left and right with respect to the filled circles, and open circles at $\ell > 2000$ are omitted.

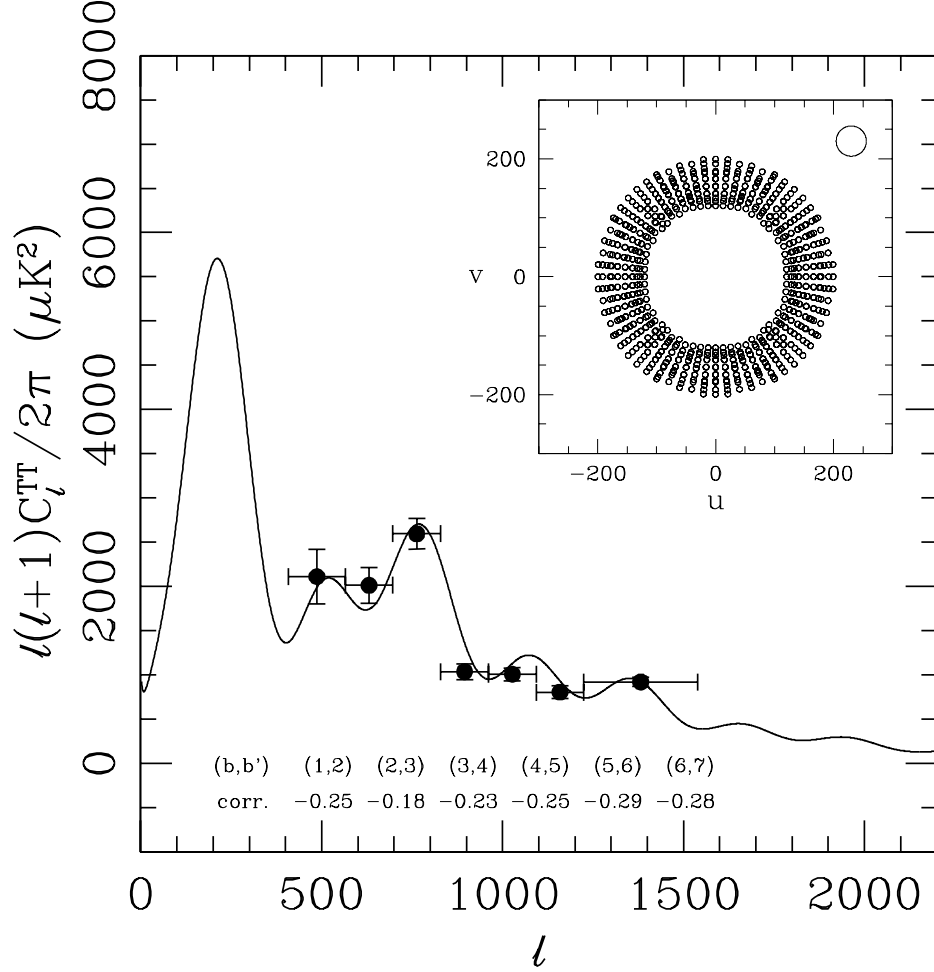


Fig. 3.— The CMB temperature anisotropy power spectrum estimated from 30 mock observations by a two-element interferometer ($D = 20$ cm, two channels with $\Delta\nu = 20$ GHz whole bandwidth centered at 95 GHz). The dish separation changes from 40 cm to 60 cm, and the platform is rotated to obtain uniform visibility samples. The distribution of visibilities in the uv -plane is shown in the upper right box. In the upper right corner of the box, the primary beam is shown as a circle with diameter $\Delta u_{\text{fwhm}} = 51.2$. Except for the first ($\Delta u = 25$) and the last ($\Delta u = 50$) bands, the band width of the intermediate five bands is chosen to be $\Delta u = 21$ ($\Delta\ell = 132$). The band power correlations between neighboring bands are also given at the bottom of the figure.

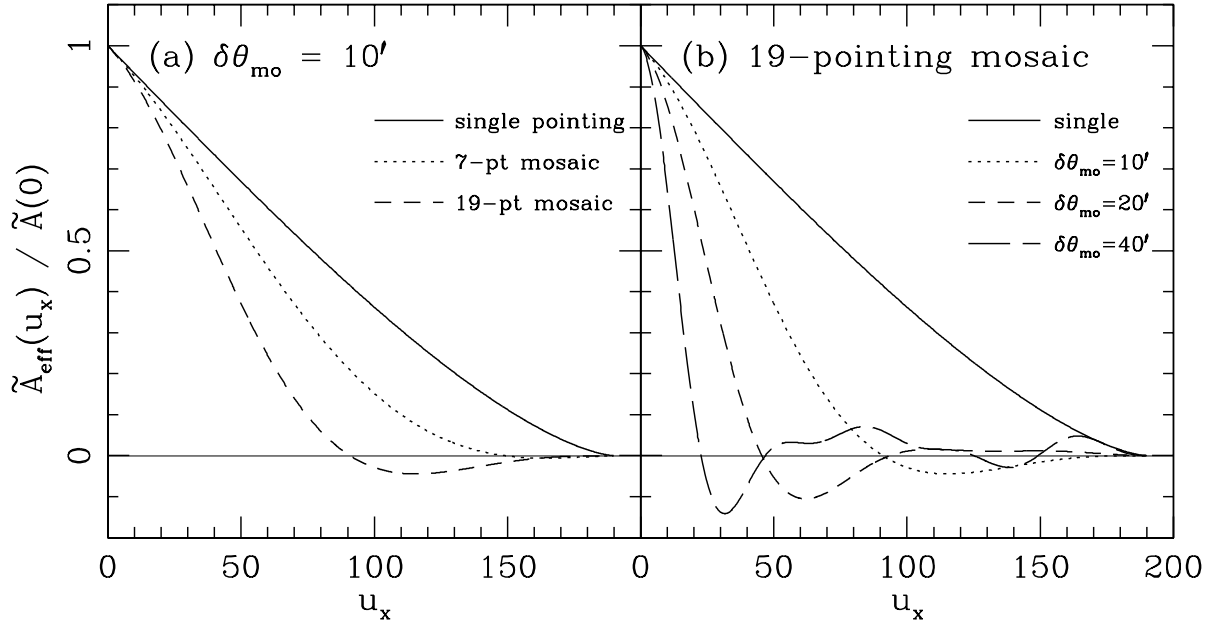


Fig. 4.— Effective beam patterns expected (a) in a single pointing observation (solid curve) and 7- and 19-point hexagonal mosaicking (dotted and dashed curves) with pointing separation $\delta\theta_{\text{mo}} = 10'$, and (b) in 19-point hexagonal mosaics with pointing separations of $\delta\theta_{\text{mo}} = 10'$, $20'$, and $40'$. The pattern of the hexagonal mosaic is similar to that of the AMiBA dishes shown in Figure 1a. Since the hexagonal configuration makes the imaginary components of the individual beam patterns along the u_x and u_y axes cancel with one another, the effective beam patterns are real functions.

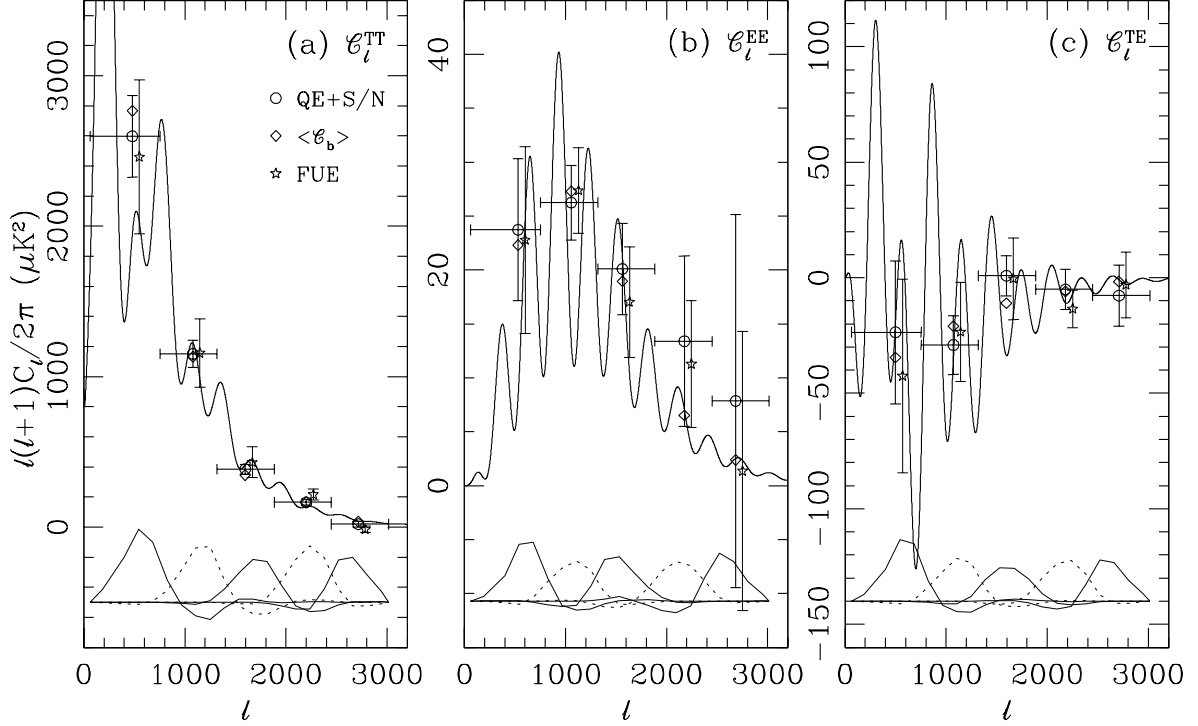


Fig. 5.— Band power estimates for (a) the temperature, (b) E -polarization, and (c) TE cross-correlation power spectra measured from the AMiBA 19-pointing hexagonal mosaic mock observation ($n_f = 10$, $t_f = 22^{\text{h}}7 \times 19$, and $\delta\theta_{\text{mo}} = 15'$). Open circles with error bars are the results of the quadratic estimator (QE) and the signal-to-noise eigenmode analysis (S/N). For each band, the band power expectation value $\langle \mathcal{C}_b \rangle$ (denoted by an open diamond) and the corresponding band power window function $f_\ell^b \equiv W_\ell^b/\ell$ (denoted by a solid or a dotted curve in the bottom region) are also shown. The ℓ -location of each band power (ℓ_{eff}) is found from $\ell_{\text{eff}} = \sum_\ell \ell f_\ell^b / \sum_\ell f_\ell^b$ (Bond et al. 1998). The band power estimates obtained by the fast unbiased estimator (FUE), right-shifted with respect to ℓ_{eff} and denoted by open stars, are consistent with those of the quadratic estimator. The FUE error bars are estimated from 30 simulations (see §5).

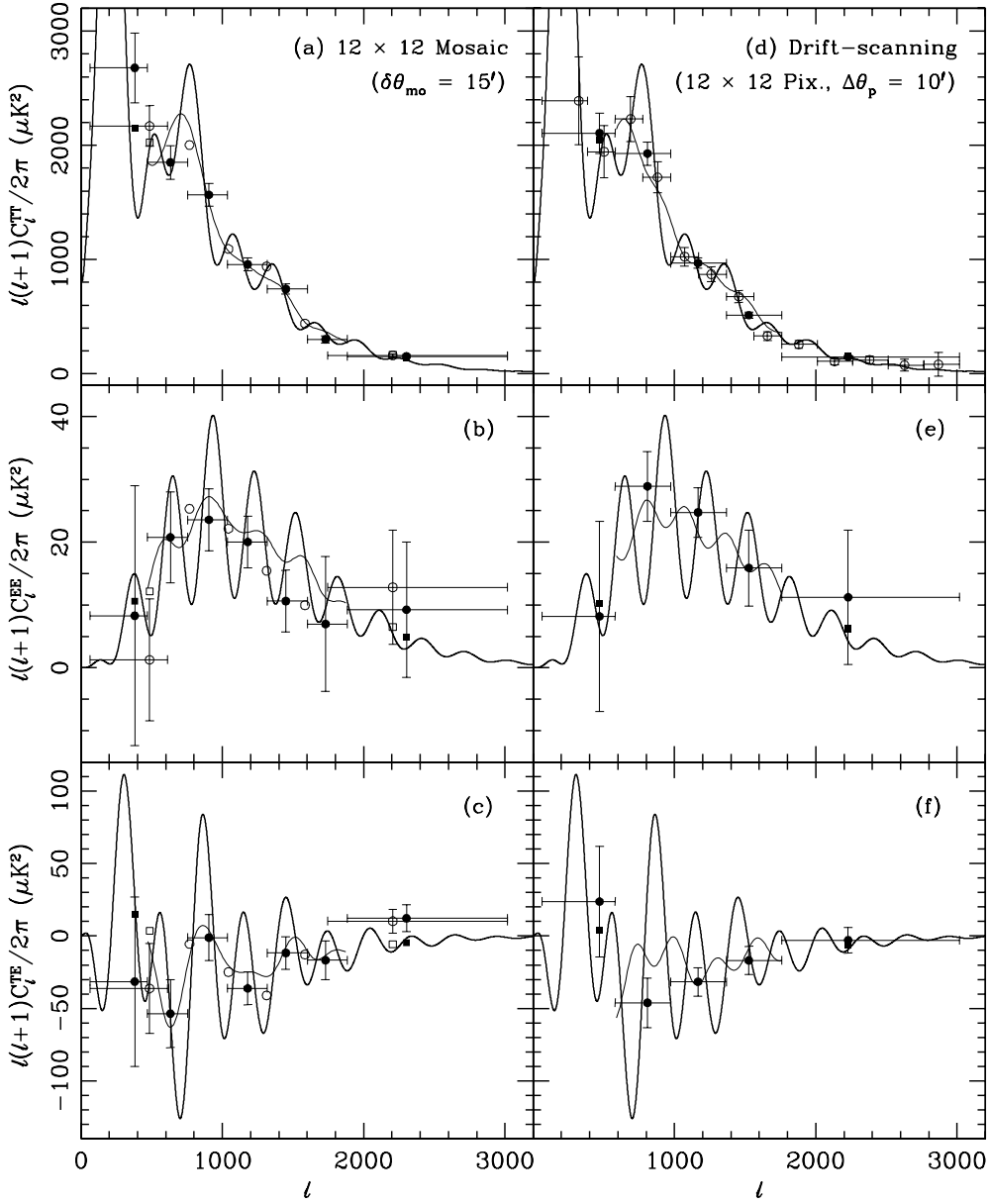


Fig. 6.— (a) Temperature, (b) E -polarization, and (c) TE cross-correlation power spectra measured from an AMiBA 12×12 mosaicking observation with $\theta_{\text{opt}} = 3^\circ$, $n_f = 5$, and $\delta\theta_{\text{mo}} = 15'$ for 6 months. Band powers are measured at two sets of band centers (filled and open circles) shifted by a half of the band width with respect to each other. Band power estimates from the data obtained by the AMiBA drift-scanning strategy ($\theta_{\text{opt}} = 2^\circ$, $n_f = 12$, and $t_{\text{tot}} = 6$ months) followed by the 12×12 pixelization with $\Delta\theta_p = 10'$ are shown in (d), (e) and (f). Open circles in the panel (d) are the temperature power spectrum measured with the band width ($\Delta u = 31.25$) twice smaller than that of the filled circles. The location of each band power is estimated using the window function defined in equation (37). Thick curves are the Λ CDM model power spectra. The model power spectra smoothed by a box of band power width ($\Delta u = 45$ for mosaicking, and $\Delta u = 62.5$ for drift-scanning) weighted by the window function are also shown (thin curves, and filled and open squares).